Dielectric Materials in Magnetic Resonance

A.G. WEBB

Department of Radiology, C.J. Gorter Center for High Field MRI, Leiden University Medical Center, Leiden, The Netherlands

ABSTRACT: High permittivity materials find extensive use in high frequency communications devices due to their small size (compared to lumped element circuits), low losses and physical robustness. Recently, these types of materials have been applied in high field magnetic resonance imaging, based upon earlier work in electron paramagnetic resonance. This review article describes the basic properties of high permittivity materials, how they can be formed into both discrete resonators and also into deformable water-based suspensions, and how these different structures can be used to improve many aspects of high frequency magnetic resonance. Concepts Magn Reson Part A 38: 148–184, 2011.

KEY WORDS: dielectric; permittivity; RF coils; high field MRI

1. INTRODUCTION – WHAT IS A DIELECTRIC MATERIAL?

With the continuing trend towards ever higher magnetic fields, whether for high resolution and solid state nuclear magnetic resonance (NMR), human and animal magnetic resonance imaging (MRI), or electron paramagnetic resonance (EPR), high permittivity materials are finding increasing utility in producing and shaping the electromagnetic (EM) fields used for pulse transmission and signal reception.

The fact that high permittivity materials are efficient magnetic field storage devices suggests that they could be used in place of the more traditional conductor-based radiofrequency (RF) coils, particularly for high frequency applications. An example is shown in Figure 1(a). Alternatively, the incorporation of high dielectric materials into a conventional RF probe (for example, either by providing a dielectric liner to the coil, or by filling the space between coil and shield) can significantly change the distribution of magnetic and electric fields within the sample. Finally, the placement of "pads" of high dielectric material around the sample, in particular human subjects in high field (7 T and above) MRI systems, can be used to "tailor" the distribution and/or increase the homogeneity of the magnetic component of the RF field. A photograph of such "dielectric pads" is shown in Figure 1(b).

This review article first considers the basic properties of dielectrics at the molecular level to explain why certain materials have very high permittivities, and the behavior of the permittivity as a function of frequency. The low-frequency characteristics of dielectrics in capacitors, and the high frequency behavior in terms of conduction and displacement currents are then discussed. The design, construction and characterization of dielectric resonators follows with a brief review of the literature in terms of their applications to EPR and high field MR microimag-

Received 24 March 2011; revised 22 May 2011; accepted 20 June 2011

Correspondence to: Andrew Webb; E-mail: a.webb@lumc.nl

Concepts in Magnetic Resonance Part A, Vol. 38A(4) 148–184 (2011)

Published online in Wiley Online Library (wileyonlinelibrary.com). DOI 10.1002/cmr.a.20219

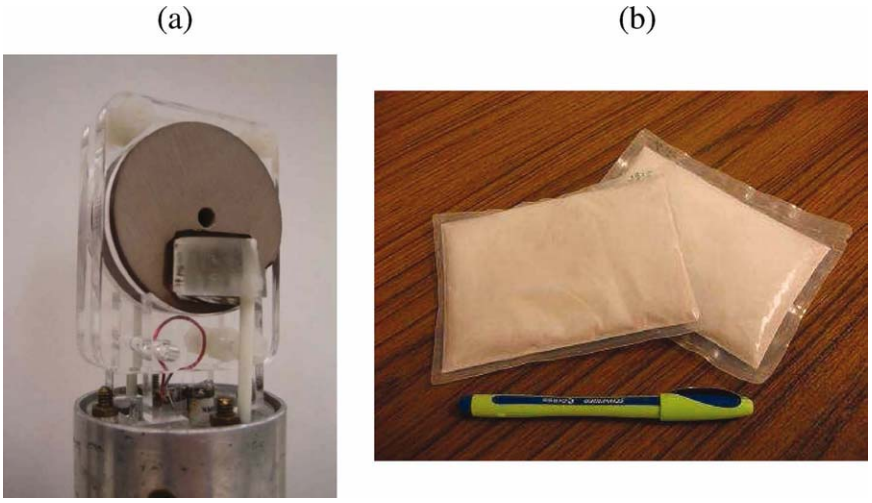

Figure 1 (a) A ceramic dielectric resonator made from sintered and pressed calcium titanate powder, designed for operation at 14.1 T (600 MHz). (b) Dielectric pads consisting of a suspension of calcium titanate powder in deuterated water, used for human imaging at 7 T (298.1 MHz).

ing. Next, the incorporation of high dielectric materials into high field MRI of humans is discussed. Finally, some projected ideas about future applications of high permittivity materials in MR are provided. The material covered particularly with respect to the role of dielectric materials in basic electromagnetics, can be supplemented by classical texts such as Kraus and Fleisch (*1*).

2. MATERIAL PROPERTIES OF DIELECTRICS

All materials have an absolute measure of permittivity (ε), and also a relative permittivity (ε_r) which is measured relative to that of vacuum ($\varepsilon_0 = 8.854 \times 10^{12}$ F/m):

$$\varepsilon_r = \frac{\varepsilon}{\varepsilon_0} \qquad [1]$$

Values of ε_r range from 1 to 10 for many plastics, 10–100 for polar solvents including (very importantly for MR applications) water, 100 to several thousand for inorganic compounds such as perovskites ("Perovskites—Inorganic Materials with High Permittivities" section), and above 10,000 for specialized materials which exhibit what is known as "giant permittivity" ("New Materials with Very High Permittivities" section). Permittivity is a complex quantity, i.e., it has both real (ε') and imaginary (ε'') components, and is often temperature and frequency dependent.

A dielectric material is one that can store energy when an external electric field is applied. Small displacements of atoms/ions and/or orientation of these atoms/ions within the material lead to "polarization." To what extent a material can be polarized in this way is expressed by its permittivity or dielectric constant. Although the two terms are technically equivalent and interchangeable, the term permittivity is preferred since it does not imply a constant value which is independent of external parameters such as frequency and temperature, which is not the case.

Materials with a high permittivity find extensive use within satellite, microwave and RF devices. They form components of filter, oscillator and mixer circuits, as well as many others in which a resonant structure is required. They are characterized by having low losses which aids in constructing narrowband filters for both transmission and reception, and have very similar frequency characteristics to waveguide filters, for example, but are much smaller in size due to the high permittivity of the materials involved. High permittivity materials are generally formed into rectangular, cylindrical or (hemi-) spherical resonant structures, acting effectively as "storage" or "concentrators" of both electric and magnetic fields. In addition to forming circuit components, they can also be used as very small transmission devices in the form of dielectric resonator antennas.

Dielectric materials are also used in the construction of capacitors, and indeed for most engineers the most common place in which dielectrics are found in MR is in the nonmagnetic capacitors that are used to tune and impedance match RF coils. Such nonmagnetic capacitors are produced by a number of companies worldwide. In addition to high permittivity, these materials must have a high breakdown voltage,

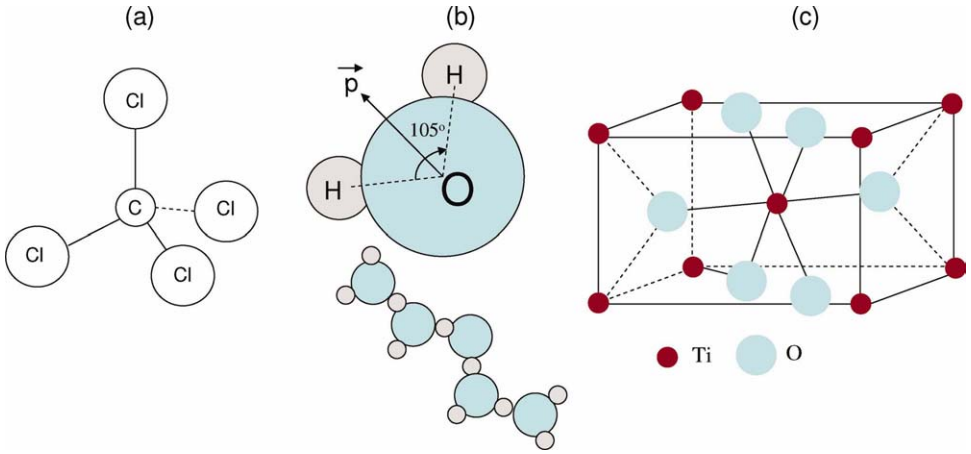

Figure 2 Three different molecules with (left) zero dipole moment, (centre) a high dipole moment in a polar molecule, also showing the extensive hydrogen bonding in the bulk material, and (right) a high dipole moment in an inorganic structure.

high mechanical stability, and have a permittivity which is as independent of temperature as possible.

Electric Dipole Moments and Polarizabilities of Materials

To illustrate the fundamentals of dielectric materials, consider three different molecules shown in Figure 2: carbon tetrachloride (CCl_4), water, and titanium dioxide. The polarity of a molecule can be quantified in terms of an electric dipole moment (**p**). For two charges q (Coulombs), which are separated by a position vector **d**, the value of **p** is given by:

$$\vec{p} = q\vec{d} \qquad [2]$$

The dipole moment has units of Debyes, with one Debye equal to 3.33×10^{-30} Coulomb metres. For a symmetric nonpolar compound such as CCl_4 shown in Figure 2(a), the centres of gravity of the positive and negative charges are identical, and therefore there is zero dipole moment. In contrast, water has a large dipole moment (1.85 Debyes) due to the strong electronegativity of the oxygen atom relative to the hydrogen, as well as a highly nonsymmetric molecular geometry, as shown in Figure 2(b). Another class of materials with high electric dipole moments are inorganic compounds containing titanium oxides: the titanate unit cell is shown in Figure 2(c). As discussed in "Perovskites—Inorganic Materials with High Permittivities" section, the high permittivity (80–100) arises from molecular distortions within the unit cell.

Appendix A Table A1 lists electric dipole moments for a small selection of materials. Considering the simple chemical solvents shown in the Appendix A Table A1, it is apparent that the more polar the substance the greater the dipole moment. However, even compounds such as CCl_4 and C_6H_6, which have zero dipole moment, do have a relative permittivity which is greater than that of vacuum. Therefore, in addition to the dipole moment, there must be a second component to the permittivity, described below, which is related to the polarizability.

As mentioned earlier the dielectric properties of materials arise from their "reaction" to an applied electric field. Depending upon the particular molecule there are a number of different mechanisms that can give rise to an induced (and overall increased) electric dipole moment. The relationship between the induced dipole moment ($\boldsymbol{p}_{ind}$) and the electric field ($\boldsymbol{E}$) is quantified via the polarizability, α:

$$\vec{p}_{ind} = \varepsilon_0 \alpha \vec{E} \qquad [3]$$

There are many mechanisms contributing to a compound's polarizability, the main ones of which are listed below, and are shown schematically in Figure 3.

Electronic Polarizability. Consider the effects of an electric field on the spherical orbital of an electron. The electrons experience a force (F) given by $F = -eE$, and as a result the orbital is spatially distorted, as shown in Figure 3(a). The positive and negative charges are no longer spatially coincident and this causes an electrostatic dipole moment ($\boldsymbol{p}_{elec}$) to be formed with a value given by:

$$\vec{p}_{elec} = \varepsilon_0 \alpha_{elect} \vec{E} \qquad [4]$$

where α_{elect} is termed the electronic polarizability.

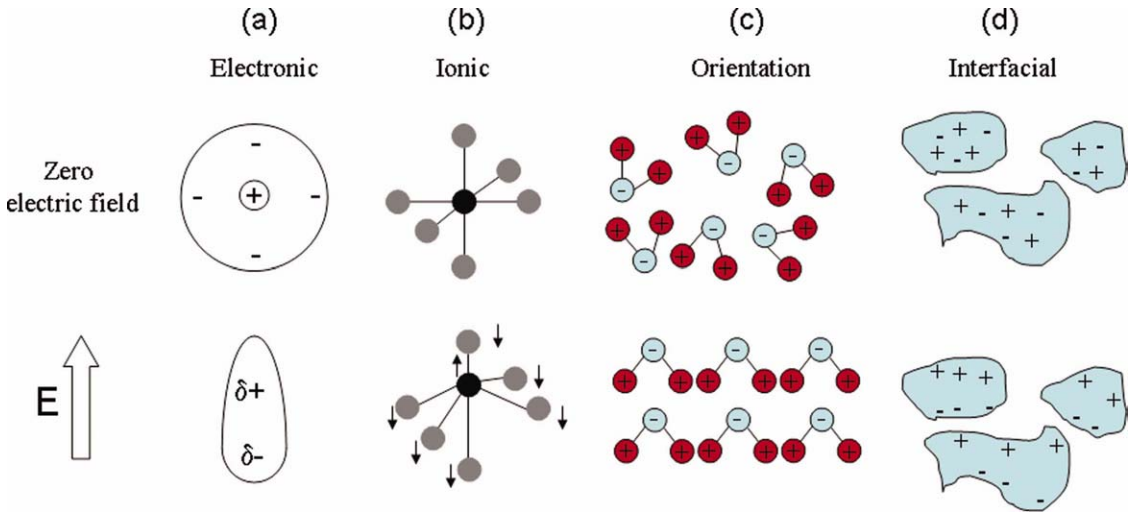

Figure 3 Schematic illustration of the four most important polarizability mechanisms.

Ionic (or Atomic) polarizability. Refers to the movement of atoms or ions within the lattice, again caused by the external electric field. As shown schematically in Figure 3(b) this motion can create an electric dipole moment in symmetric molecules, and can significantly increase its size in molecules with a permanent electric dipole moment. An ionic dipole moment is defined in terms of the ionic polarizability, α_{ionic}, in exactly the same way as in Eq. [4].

Orientation (or Molecular or Dipole) polarizability. Refers to the phenomenon that if a polar molecule with a permanent dipole moment ($\boldsymbol{p}_o$) experiences an external electric field, then a torque (Γ) is created which attempts to align the dipole with the direction of the field. The torque produced is given by:

$$\vec{\Gamma} = \vec{p}_o \wedge \vec{E} \qquad [5]$$

The effect of the torque is to distort the molecule, which produces an additional component $\boldsymbol{p}_{\text{orient}}$ in the direction of the electric field, with a value proportional to an orientational polarizability, α_{orient}. Figure 3(c) shows this effect schematically for water molecules, for which the orientation polarizability is particularly strong.

Interfacial (or Space-Charge) polarizability. Refers to the action of charge carriers that can migrate short distances within the material, as shown in Figure 3(d). Application of an electric field impedes the motion of these carriers, resulting in a distortion of the macroscopic field. In analogy to previous equations, one can define an interfacial polarizability, $\alpha_{\text{interface}}$.

Assuming that the four contributions to polarization are independent, then the total polarizability of the dielectric material is simply given by the sum of the four separate mechanisms.

$$\alpha = \alpha_{\text{elec}} + \alpha_{\text{ionic}} + \alpha_{\text{orient}} + \alpha_{\text{interface}} \qquad [6]$$

and the corresponding dipole moment by:

$$\vec{p} = \varepsilon_0 \vec{E}(\alpha_{\text{elec}} + \alpha_{\text{ionic}} + \alpha_{\text{orient}} + \alpha_{\text{interface}}) \qquad [7]$$

In fact, many of the dielectric materials described in this article are "directional dielectrics," i.e., the polarizatibility is not the same in each direction, and therefore a full description of the dipole moment is determined by the polarizability in tensor form:

$$\vec{p} = \varepsilon_0 \overleftrightarrow{\alpha} \vec{E}, \quad \overleftrightarrow{\alpha} = \begin{bmatrix} \alpha_{xx}\alpha_{xy}\alpha_{xz} \\ \alpha_{yx}\alpha_{yy}\alpha_{yz} \\ \alpha_{zx}\alpha_{zy}\alpha_{zz} \end{bmatrix} \qquad [8]$$

where α_{xy}, for example, refers to the polarizability in the x-direction induced by the y-component of the electric field. For simplicity, the remainder of the article assumes that the direction-dependence of the polarizability is small enough to be neglected.

For MR and EPR applications it is important to consider the frequency dependence of these mechanisms. In addition to different materials having very different contributions from the respective polarizabilities, these contributions are also highly frequency dependent. Interfacial polarization typically has a strong contribution only at very low frequencies (sub-MHz), whereas orientation, ionic and

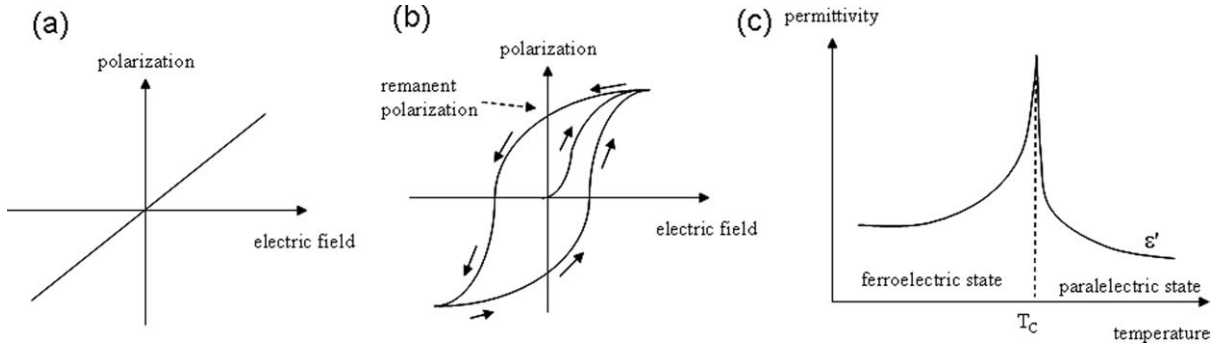

Figure 4 (a) Polarization of a paraelectric material is linear with the applied electric field. (b) Schematic of the hysteresis loop associated with ferroelectric behavior. (c) The temperature dependence of the permittivity near the ferroelectric/paraelectric transition at the Curie temperature.

electronic (in increasing order of frequency) can have substantial contributions in the RF and microwave frequency ranges. For frequencies in the hundreds of MHz range (relevant to high field MR applications), the two dominant mechanisms are ionic and electronic. A short summary of dielectric relaxation is presented in Appendix B.

In a particular sample, the average electric dipole moment per unit volume is termed the polarization (***P***).

$$\vec{P} = N\vec{p} = N\alpha\vec{E} \qquad [9]$$

where N is the number of molecules per unit volume. One can relate the polarization to the relative permittivity of a material via its electric susceptibility χ_e (an analogue to magnetic susceptibility). In the first step, the relationship between the polarization and total electric field is given by:

$$\vec{P} = \varepsilon_0\chi_e\vec{E} \qquad [10]$$

The electric displacement field (***D***) is defined by:

$$\vec{D} = \varepsilon_0\vec{E} + \vec{P} = \varepsilon_0(1 + \chi_e)\vec{E} \qquad [11]$$

D can also be expressed as:

$$\vec{D} = \varepsilon\vec{E} = \varepsilon_r\varepsilon_0\vec{E} \qquad [12]$$

and so:

$$\varepsilon_r = 1 + \chi_e = 1 + \frac{\vec{P}}{\varepsilon_0\vec{E}} \qquad [13]$$

As would be expected, the larger the polarization the higher the relative permittivity, with a linear relationship exhibited for high values of polarization.

Paraelectric, Ferroelectric and Piezoelectric Properties of Dielectrics

Dielectric materials can also be defined further in terms of being paraelectric, ferroelectric and/or piezoelectric. In a paraelectric material, polarization is produced by the effect of an external applied electric field, but the polarization is not retained when the electric field is removed, as shown in Figure 4(a). Mechanistically, any change in ionic displacement, for example, returns to zero when the electric field is switched off. In contrast, in a ferroelectric material the polarization is retained when the electric field is turned off, and ferroelectric materials display a hysteresis effect in the polarization, as shown in Figure 4(b). The applied electric field orders the permanent electric dipoles within the material into domains, and also aligns the domains themselves to produce a high polarization. If the electric field is strong enough then the material becomes saturated, with all the dipoles fully aligned.

Many dielectrics can exist either in the paraelectric or ferroelectric states depending upon the temperature relative to the Curie temperature (T_c). Above T_c a material is paraelectric, whereas below T_c it is ferroelectric. As shown in Figure 4(c) the permittivity changes rapidly close to the Curie temperature.

Ferroelectric materials, such as barium titanate (covered in the next section), are typically crystalline, and have high permittivities (values over 1,000) which are highly temperature and frequency dependent: it should be noted that the prefix "ferro-" is a historical misnomer in that most ferroelectric materials do not, in fact, contain iron. Paraelectrics have lower permittivities, which are much more constant with respect to temperature and frequency than ferroelectrics. Examples include tantalum oxide ($\varepsilon_r = 23$) and niobium oxide ($\varepsilon_r = 40$).

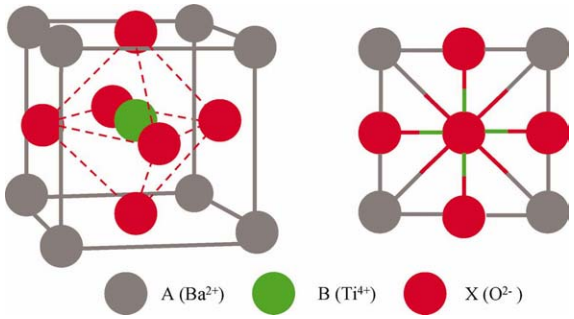

Figure 5 General structure of the perovskite, ABX_3, with the particular example of barium titanate shown. The barium atoms form a cubic structure, with the oxygen atoms forming a tetragonal structure.

It should be noted that many high dielectric materials are also piezoelectric. These types of materials produce a voltage when pressure is applied, and in a reciprocal manner an applied voltage causes the material to change physical dimensions at the same frequency at which the voltage is applied. These materials are used extensively in ultrasound transducer design for medical applications and nondestructive testing.

Perovskites—Inorganic Materials with High Permittivities

Most applications of dielectrics in MR use materials with high permittivity ($\varepsilon_r > 100$). One of the most important classes of high permittivity materials is the perovskites, named after a renowned Russian mineralogist, Count Lev Alexevich von Perovski. This class of compounds has an ABX_3 chemical structure, with A being a large metal cation which is close-packed in layers with X ions (usually oxygen). B is a smaller metal ion positioned in octahedrally-coordinated holes between the close-packed layers: the general structure of a perovskite is shown in Figure 5 (*2*).

Barium titanate ($BaTiO_3$) was the perovskite first investigated in great detail, with early applications in radar systems. The general structure is a network of corner-linked anion octahedra, with the smaller cation filling the octahedral holes, and the larger cation filling the dodecahedral holes, as shown in Figure 5. Barium titanate exists in the paraelectric cubic phase above its Curie temperature of 120°C, while between 0 and 120°C the ferroelectric tetragonal phase is stable. The high permittivity of the material arises from a structural change in which the central Ba and Ti cations are displaced with respect to the oxygen ions, the resulting reduction in symmetry leading to the formation of large electric dipoles. Substitution of different metals for Ba can change the Curie temperature significantly. For example, replacing Ba with strontium in the A-site reduces the Curie temperature, whereas substituting Pb for Ba increases it. The dielectric properties also depend on the grain size of the material, with the highest permittivity found for very small (sub-micron-sized) ceramics. This has been attributed (*3*) to the internal stresses for the smaller particles being higher than for larger particles.

Major changes in structure are shown by sharp jumps in the permittivity as a function of temperature, as shown in Figure 6. Of particular interest for MR applications is its behavior between room temperature and its Curie temperature of 120°C. Above T_c the thermal motions of the Ti atoms are sufficient to be able to retain the ideal cubic perovskite structure. However, below T_c the residual strain in the unit cell is too large, and the structure distorts.

The ionic distortion in $BaTiO_3$ is shown in more detail in Figure 7. As shown in Figures 7(a,b) below the Curie temperature, the central Ti atom shifts off-centre, as well as smaller shifts occurring for the barium atoms. In the perovskite structure all of the octahedra are connected only at their corners and are fixed in place by the A cations, so an efficient coupling between the octahedra arises from any disturbance. Any displacement of a titanium ion has an effective feedback mechanism via the oxygen lattice which causes adjacent titanium ions to move in the same direction, as shown in Figure 7(c). As described by Hippel (*4*) as the titanium ion A moves towards O_1, the dipole moment between the two ions becomes stronger and that between A and O_2 weaker. Therefore, O_1 moves towards A and O_2 away from it. The result of this is that the two Ti ions, B and C, both follow the motion of A. The titanium ions on the side (D, E and their counterparts in the front and back of the plane) also move in the same direction due to the coupling O ions (O_3, O_4, etc.) moving downwards due to repulsion from O_1. The role of the

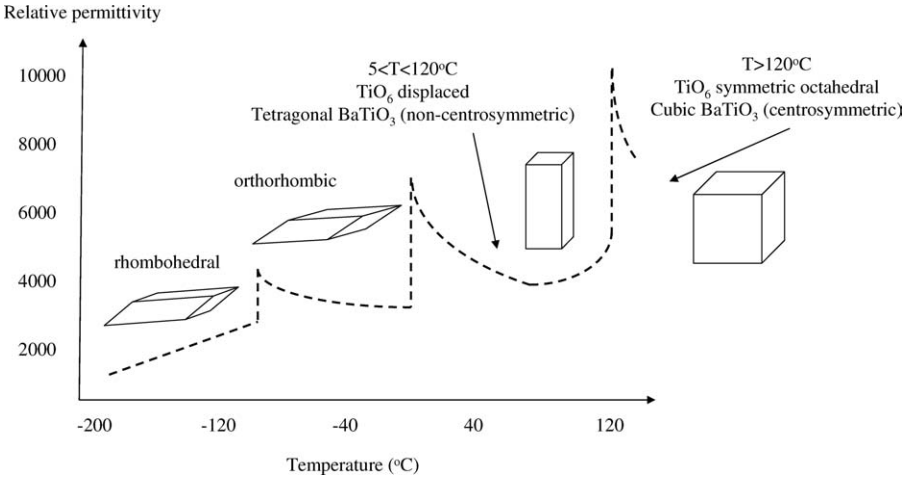

Figure 6 Plot of relative permittivity vs. temperature for barium titanate, together with the structural changes corresponding to each sharp jump in value.

barium ions is to hold the oxygen ions in place, thus reducing the feedback mechanism that could otherwise lead to the splendidly named "Mosotti catastrophe." The higher the bond strength between the large metal ion and the oxygen, the more the feedback damping. This explains the importance of the large metal ion in the variations in permittivity values for different perovskites.

The stability of a particular perovskite phase can be analyzed using a tolerance factor, t. For the A, B, and O ions to be in "physical" contact simply geometry dictates that:

$$R_A + R_O = \sqrt{2(R_B + R_O)} \qquad [14]$$

where R represents the radii of the corresponding ions. The tolerance factor is simply defined as:

$$t = \frac{R_A + R_O}{\sqrt{2(R_B + R_O)}} \qquad [15]$$

If the value of t is unity, then a perfect cubic cell can be formed. For $t > 1$ the A cations are relatively large, the B cations relatively small, and so the B ions have more "space" to move. The opposite is true for $t < 1$. For example in $CaTiO_3$, a material which has been used extensively in MR applications, $t = 0.97$ and the molecule is orthorhombic.

New Materials with Very High Permittivities

New materials such as calcium copper titanate (CCTO), the structure of which is shown in Figure 8, and lanthanum strontium nickelate have what is termed a "giant permittivity." CCTO is a perovskite-like body-centred cubic oxide. Ca and Cu ions reside at the A-sites, while Ti cations occupy the B-site and

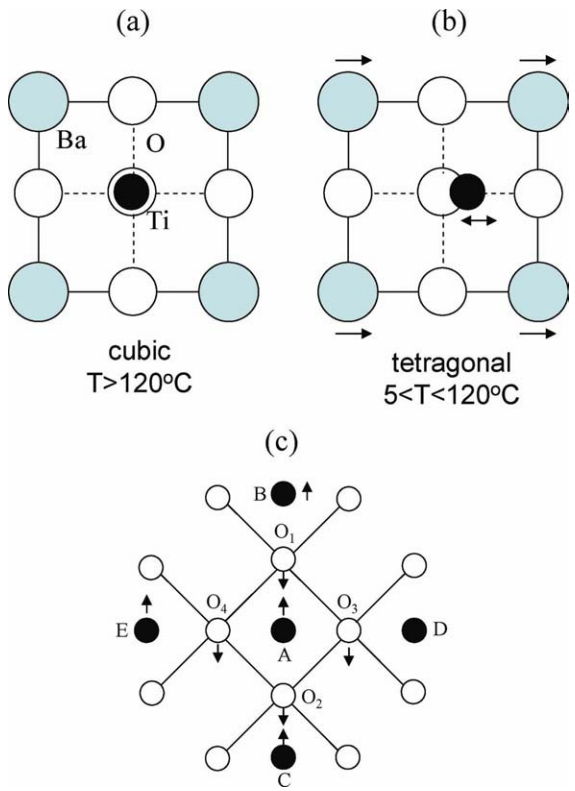

Figure 7 Movement of ions above (a) and below (b) the Curie temperature for barium titanate. (c) Schematic of the feedback coupling between the movement of Ti ions via intermediate O atoms.

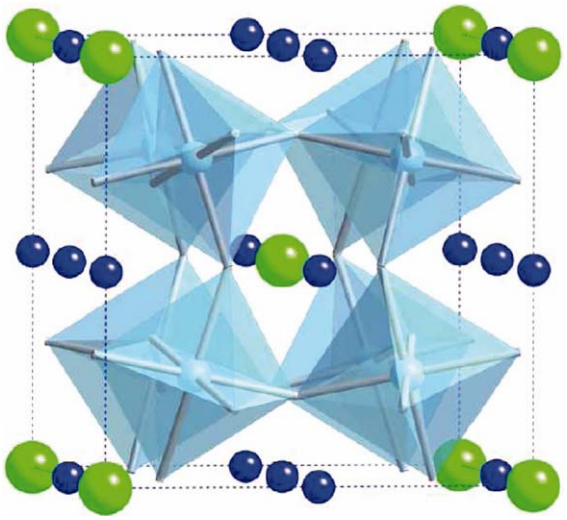

Figure 8 The unit cell of calcium copper titanate, with calcium ions in green, copper ions in blue and TiO_6 octahedra displaces as semisolid representations.

O anions the X sites. The permittivity is essentially temperature and frequency independent, with values from 10,000 to 100,000.

Another giant dielectric material is based on lanthanum, $La_{2-x}Sr_xNiO_4$. The high permittivity is thought to be due to charge ordering in these structures which leads to thermally activated small polaronic hopping. Electrical conduction in transition metal oxides occurs through strong coupling between electrons and phonons (from lattice vibrations), which create so-called polarons. These polarons can jump from one site (leaving a hole behind) to another (filling a hole) at a temperature greater than one-half the Debye temperature (the temperature where charge ordering is observed in the structure). In the case of Ti-based giant permittivity materials, the electrons from Ti^3 can jump into adjacent Ti^4 sites, which involves antisymmetric displacement of bridging oxygen atoms, which causes a large overall polarization in the whole structure which in turn leads to the giant permittivity.

3. DIELECTRIC MATERIALS, COMPLEX PERMITTTIVITY AND DISPLACEMENT CURRENTS IN CAPACITORS

As mentioned in the introduction, a common use of dielectric materials is in capacitors. The capacitor is also a simple vehicle for introducing the concept of complex permittivity. In the general case of a capacitor being charged up by a voltage source with associated charging current:

$$Q = CV = \frac{\varepsilon_r \varepsilon_0 A}{d} V \qquad [16]$$

where Q is the stored charge, A the cross-sectional area of the parallel plates, d the distance between the plates, and V the charging voltage. A material with high permittivity gives a large stored charge for a given driving voltage, as shown in Figure 9. The permittivity of several dielectrics used in capacitors include: barium titanate (1,700), alumina (Al_2O_3, 9), tantalum oxide (Ta_2O_5, 22), strontium titanate (2,000), and lanthanum oxide (La_2O_3, 30). For a more extensive list see reference (*5*). A high dielectric material placed between the plates of a capacitor causes the electric field inside the capacitor to be reduced for a given charge on the plates. This is because the molecules of the dielectric material are polarized by the electric field, and they align in a configuration that sets up inside the dielectric a secondary electric field which is opposite in polarity to

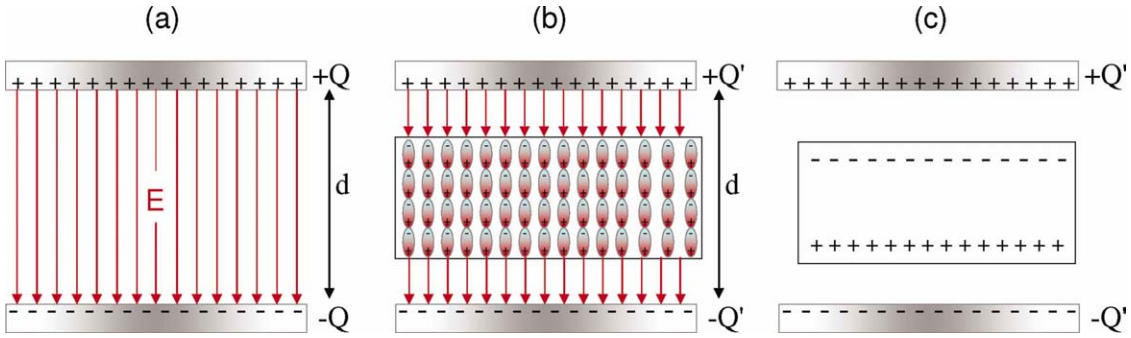

Figure 9 (a) A parallel plate capacitor with air between the two plates. There is a large electric field between the two plates. (b) The same capacitor with a high permittivity material sandwiched in between the plates. (c) The net effect of the dielectric material is to reduce the electric field by a factor ε_r.

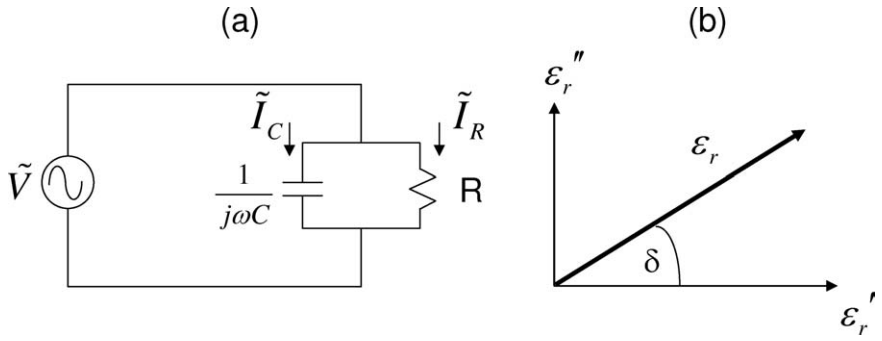

Figure 10 (a) Circuit diagram of a lossy capacitor. (b) The loss tangent (tan δ) in relation to the real (ε′) and imaginary (ε″) components of the permittivity.

the field from the capacitor plates. For a DC voltage, charge builds up between the plates of the capacitor and eventually no current flows through the capacitor. However, for MRI purposes we are interested not in a DC voltage but in alternating (cosinusoidal) voltages, and associated alternating currents, magnetic fields and electric fields. Assuming a driving voltage given by:

$$V(t) = V_0 \cos \omega t \qquad [17]$$

The well-known expressions for current, electric field, and impedance are given by:

$$\begin{aligned} I(t) &= -\omega C V_0 \sin \omega t \\ E(t) &= \frac{V(t)}{d} = \frac{V_0 \cos \omega t}{d} \\ Z &= \frac{V(t)}{I(t)} = \frac{1}{j\omega C} = -j\frac{1}{\omega C} \end{aligned} \qquad [18]$$

Under the influence of an alternating driving voltage the direction of the electric field reverses polarity at the frequency of the voltage source. The electric field builds up from zero to maximum in one direction and then collapses back to zero. The field then builds up to a maximum in the opposite direction and then returns to zero.

An apparent problem is that the dielectric is an insulator and therefore no current should pass through it, and yet we know that alternating currents do pass through capacitors. The key explanatory concept is that there are two different types of current, namely conduction and displacement currents. Conduction currents refer to the conventional passage of electrons through a material, and this type of current indeed cannot flow through a pure insulator. In contrast, a displacement current is one that is produced by the small (reversible) variations in the position of the atoms and ions within the dielectric material: thus a displacement current produces no net flow of ions or electrons through the material. The displacement current density (J_D) is proportional to the time-derivative of the electric field:

$$J_D = \varepsilon_0 \varepsilon_r \frac{\partial E}{dt} \qquad [19]$$

Intuitively the displacement current must be equal to the conduction current, and this is relatively easy to show mathematically:

$$J_D = \varepsilon \frac{d\vec{E}}{dt} = -\varepsilon\omega \frac{V_0}{d} \sin \omega t \qquad [20]$$

Then the displacement current, I_D, is given by:

$$I_D = J_D A = -A\varepsilon\omega \frac{V_0}{d} \sin \omega t = -\omega C V_0 \sin \omega t = I_C \qquad [21]$$

As shown later in Section 7, displacement currents are very important in the design of dielectric pads for high field MRI.

The analysis so far has considered an ideal capacitor with no resistance and therefore no loss. However, all capacitors have some loss which can be modeled as a resistor, R_{cap}, in parallel with the ideal, lossless capacitor, as shown in Figure 10. The loss is typically specified in terms of a quality factor (Q), given by:

$$Q_{cap} = \frac{1}{\omega R_{cap} C} \qquad [22]$$

There are many ways of considering the Q value of a component or an electrical circuit. Essentially a low Q value indicates high loss, but also a large frequency bandwidth (the Q value is given by the resonance frequency divided by the full-width-half-

maximum bandwidth), and vice-versa. Q values of commercial capacitors are typically quoted as several hundreds, but for MR applications one should be aware that most of these measurements are performed at low frequencies, typically 1 MHz, and the Q value can drop very significantly with frequency.

In Figure 10 the respective currents through the capacitor and resistor are given by:

$$\tilde{I}_c = j\omega C\tilde{V}$$
$$\tilde{I}_R = \frac{\tilde{V}}{R_c} \quad [23]$$

Since losses occur in the dielectric this means that we can write the permittivity not only with a real (lossless) component ε', but also with an imaginary (lossy) component ε''.

$$\varepsilon = \varepsilon' - j\varepsilon'' \quad [24]$$

Note that a minus rather than plus sign is used for the lossy component since energy is being removed from the system by the imaginary term. The real part of the permittivity represents the energy storage, whereas the imaginary part represents the loss. The dielectric conductivity, σ_{diel}, is defined as:

$$\sigma_{diel} = \omega\varepsilon'' \quad [25]$$

The value of ε'' is important because the total power absorbed per unit volume of the dielectric is given by:

$$\text{Power} = \sigma_{diel}\frac{E_0^2}{2} = \omega\varepsilon''\frac{E_0^2}{2}\left(Wm^{-3}\right) \quad [26]$$

The loss is most commonly quantified in terms of the loss tangent (tan δ) of a dielectric, which is given by the ratio of the loss current to the charging current through the capacitor:

$$\tan\delta = \frac{\tilde{I}_R}{\tilde{I}_C} = \frac{\tilde{V}_R/R}{j\omega C\tilde{V}_0} = \frac{1}{j\omega RC} \quad [27]$$

The quantity δ is an angle, and represents the deviation from 90° describing the phase difference between the current and voltage. From Figure 10 it is also clear that:

$$\tan\delta = \frac{\varepsilon''}{\varepsilon'} \quad [28]$$

In most applications, it is desirable to keep the loss tangent as low as possible, since it effectively represents power that is dissipated in heat, therefore serving no useful purpose. The dielectric materials used in capacitors typically have tan δ values much less than 0.1.

4. EM WAVE PROPAGATION IN DIELECTRIC MATERIALS

When considering MR applications of dielectric resonators and dielectric pads, for example, one is concerned with the interaction of the dielectric material with the propagating EM fields associated with both the transmission of RF pulses and also reception of the MR signal. As EM waves propagate through dielectric materials three basic phenomena occur: (i) the EM wavelength changes, being inversely proportional to the square root of the relative permittivity, (ii) the waves are attenuated by any conductivity within the dielectric, and (iii) waves are reflected and refracted due to boundaries between materials with different permittivities: these three phenomena are shown schematically in Figure 11. In addition to induced conduction currents, the electric field causes a displacement current within a dielectric, which in turn produces a secondary magnetic field component. In human MRI the dielectric properties of different organs can produce significant inhomogeneities in the EM wave distribution, particularly at high field strengths. However, displacement currents in high permittivity "pads" can also be used to correct for some of the spatial inhomogeneities in the primary EM field, as covered in Section 7.

The electric and magnetic fields propagating in the x-direction, as shown in Figure 11(b), can be represented mathematically as:

$$E = E_0 e^{+j\omega t-\gamma x}$$
$$H = H_0 e^{+j\omega t-\gamma x} \quad [29]$$

where

$$\gamma = \alpha + j\beta = j\omega\sqrt{\varepsilon\mu} \quad [30]$$

where μ is the magnetic permeability, α is termed the attenuation factor (not to be confused with the polarizability) and β the phase factor, given by $2\pi/\lambda$. For a lossless dielectric the value of α is zero, and the E and H fields are given by:

$$E = E_0 e^{j(\omega t-\beta x)}$$
$$H = H_0 e^{j(\omega t-\beta x)} \quad [31]$$

The intrinsic impedance, Z, of a dielectric is given by:

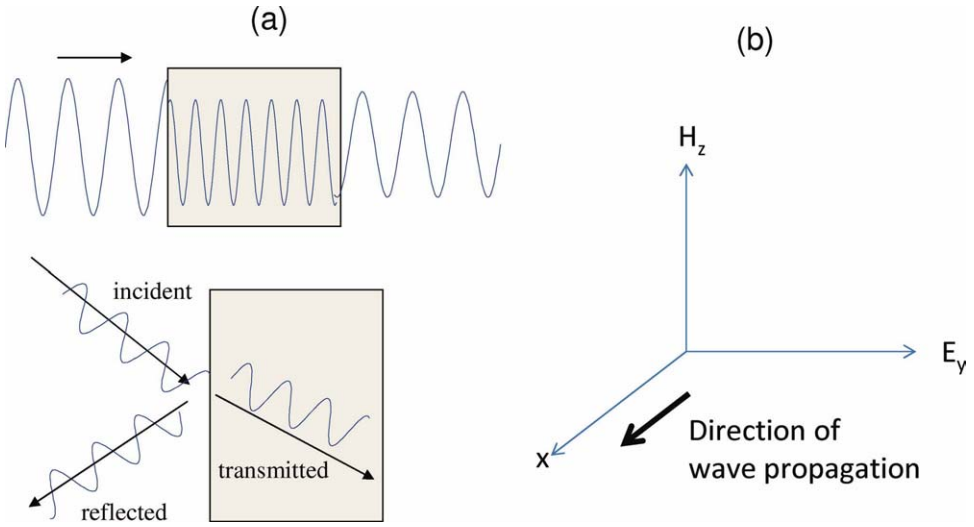

Figure 11 (a) As an EM wave enters a region of high permittivity (gray box) the wavelength decreases by a factor of $\sqrt{\varepsilon_r}$. At the boundary between materials with different permittivities part of the wave is transmitted and part reflected. (b) Convention for propagation of planar EM waves, with the *H* and *E* fields perpendicular to the direction of propagation.

$$Z = \sqrt{\frac{\mu}{\varepsilon}} \qquad [32]$$

The index of refraction, n, is defined as the ratio of the EM wavelength in vacuum (λ_0) to that in the particular dielectric material:

$$n = \frac{\lambda_0}{\lambda} = \frac{\lambda_0}{2\pi}\beta \qquad [33]$$

For a lossless dielectric:

$$n = \sqrt{\frac{\varepsilon'\mu'}{\varepsilon_0\mu_0}} \qquad [34]$$

where (μ') is the real part of the magnetic permeability:

$$\mu' = Re\{\mu_r\mu_0\} \qquad [35]$$

μ_0 is the magnetic permeability of free space, equal to $4\pi \times 10^7$ Hm^1. For most materials (with the exception of ferromagnetics which have a very high value of magnetic permeability) $\mu' \sim \mu_0$, giving the well-known formula relating the EM wavelength to material permittivity.

$$\lambda = \lambda_0\sqrt{\frac{\varepsilon_0}{\varepsilon'}} \qquad [36]$$

The wavelength within the dielectric is therefore inversely proportional to the square root of the real part of the permittivity. If the loss in the dielectric cannot be ignored, then the corresponding equation is given by:

$$\frac{\lambda}{\lambda_0} = \left[\frac{1}{2}\frac{\varepsilon}{\varepsilon_0}\left(1 + \sqrt{1 + \tan^2\delta}\right)\right]^{-\frac{1}{2}} \qquad [37]$$

which reverts to Eq. [36] in the case that $\tan\delta = 0$.

It is important to note that, despite the mathematical relationship between n and ε, since permittivity is frequency dependent the value of the refractive index which is measured at optical frequencies does not, in general, correspond to the same value of permittivity measured at microwave or radio frequencies. The values would only be exactly equal if the polarization mechanisms were the same at both frequencies: this is almost never the case. Referring back to the mechanisms outlined in Section 2, orientation polarization mechanisms, for example, are effective at RF but are much less efficient at optical frequencies.

Displacement and Conduction Currents in Dielectrics at High Frequencies

Although dielectric materials are essentially insulators they do have some conductivity, in other words they support conduction currents, at high frequencies. Such dielectric losses occur due to the physical properties of the material arising from, for example, damping forces during the repeated polarization changes due to an oscillating external electric field. These losses appear in phase with any inherent

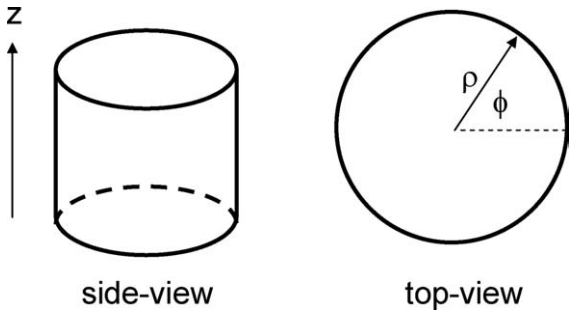

Figure 12 Axes and co-ordinate convention used for dielectric resonators

conduction current. Therefore, at high frequencies, the loss tangent includes contributions from both dielectric loss and the conduction current. The relationship between the magnetic and electric fields inside an isotropic dielectric material which has a finite conductivity, is given by one of Maxwell's equations:

$$\nabla \times H = (\sigma + j\omega\varepsilon)E \qquad [38]$$

By including conductivity and damping loss mechanisms outlined above, the modified Maxwell's equation becomes:

$$\nabla \times H = \left(\varepsilon' - j\omega\left(\varepsilon'' + \frac{\sigma}{\omega}\right)\right)E \qquad [39]$$

As mentioned earlier, the total losses therefore comprise ones from the complex permittivity and those from the small DC conductivity, resulting in an effective conductivity (σ_{eff}):

$$\sigma_{eff} = \sigma + \omega\varepsilon'' \qquad [40]$$

At high frequencies the second term on the right hand side dominates, and so often the simplification is made that:

$$\sigma_{eff} \approx \omega\varepsilon'' \qquad [41]$$

5. DIELECTRIC RESONATORS IN EPR AND MRI

The first applications of high permittivity materials were in EPR using dielectric resonators (DRs) formed from high permittivity ceramics. With operating frequencies in the 1–250 GHz range, conventional EPR detection uses cavity resonators. As mentioned in the introduction, the use of high permittivity materials can reduce the size of devices significantly. DRs use low loss ceramic structures that can store energy effectively. The ideal situation for both EPR and MR experiments is to contain as much of the magnetic energy within the structure itself. Various materials have been used for DRs for EPR including TiO_2 (rutile, $\varepsilon_r \approx 100$), $SrTiO_3$ ($\varepsilon_r \approx 300$), $BaTiO_3$ ($\varepsilon_r \approx 3{,}000$), and $Ba_xSr_{1-x}TiO_3$ ($300 \leq \varepsilon_r \leq 3{,}000$ based on the ratio of Ba to Sr). Commonly used DR geometries include rectangular, cylindrical, and annular structures. The properties of DRs and their use in EPR and MRI are described in the following sections.

Modal Distributions in Dielectric Resonators

Specific resonant modes of a DR refers to stable time-invariant electric- and magnetic-field patterns that are formed within the resonator. Cylindrical DRs have transverse electric (TE) and transverse magnetic (TM) modes, as well as hybrid electromagnetic (HEM) modes. A TE mode is defined as one whose electric field vector is normal to the direction of propagation (zero electric field in the propagation direction), a TM mode as one whose magnetic field vector is normal to the direction of propagation (zero magnetic field in the propagation direction), and an HEM mode with nonzero electric and magnetic fields in the propagation direction. Different modes are denoted by subscripts, e.g., TE_{01}, TM_{21}, and HEM_{11}. The two subscripts for each mode (TE_{mn}) denote the number of half-wavelength field variations in the ϕ and ρ directions respectively, with the convention shown in Figure 12.

In the case of a cylindrical DR pure TE and TM modes exist only when the field variations are independent of ϕ, meaning m=0 for all TE and TM modes, which must therefore be cylindrically symmetric. Figure 13 shows the distribution of electric and magnetic fields for the most commonly used mode of a cylindrical DR, the $TE_{01\delta}$ mode. The subscript δ is applied when there is less than half-a-

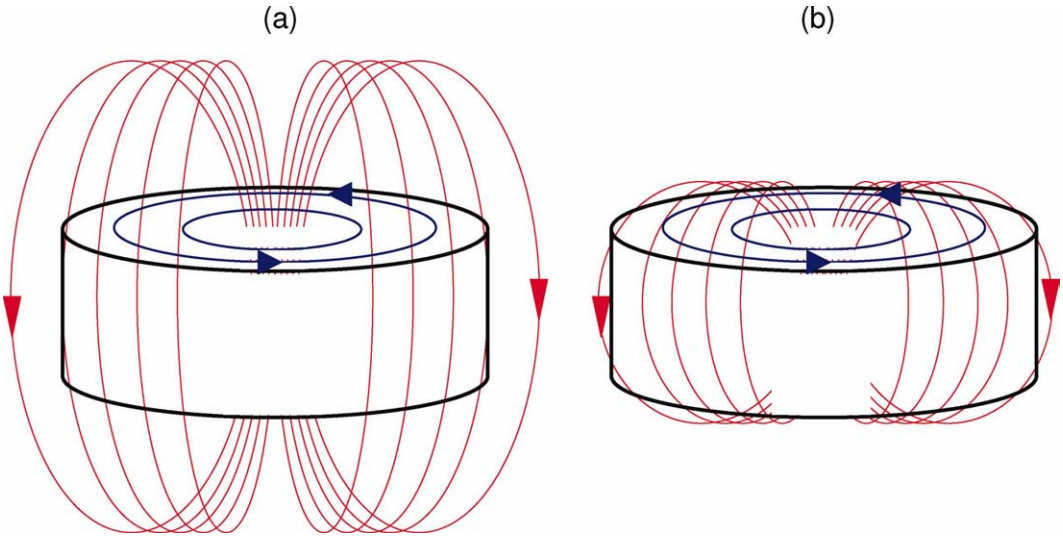

Figure 13 Schematic of the magnetic (red) and electric (blue) field lines for the $TE_{01\delta}$ mode in a solid cylindrical dielectric resonator. (a) shows the case for a DR with a low relative permittivity, in which evernescent fields protrude from the resonator, whereas in (b) the permittivity is much higher and the fields are almost entirely contained within the resonator itself.

wavelength variation in the transverse fields within the dielectric. In this mode the electric and magnetic are tangential to one another. The electric field is zero at the centre of the DR, and is almost entirely constrained within the structure of the DR.

At a dielectric-air interface one can define the plane wave reflection coefficient (Γ) as the ratio of the intensity of the EM wave reflected at the boundary divided by the intensity transmitted through the boundary. The value of Γ is given by:

$$\Gamma = \frac{\sqrt{\frac{\mu_0}{\varepsilon_0}} - \sqrt{\frac{\mu_0}{\varepsilon_0\varepsilon_r}}}{\sqrt{\frac{\mu_0}{\varepsilon_0}} + \sqrt{\frac{\mu_0}{\varepsilon_0\varepsilon_r}}} \qquad [42]$$

Since the relative magnetic permeability, μ_r, of the resonator is very close to unity, as ε_r becomes larger so does the value of Γ, approaching its maximum value of 1 as ε_r goes to infinity. Under these conditions, the EM wave is reflected back into the resonator at the boundaries, effectively storing the entire magnetic energy within the resonator, as shown in Figure 13(b).

The magnetic, $H(t)$, and electric, $E(t)$, field patterns for four lower order DR modes are shown in Figure 14. The snapshots in Figure 14 were acquired when each field was at its maximum value. The larger, darker vectors correspond to where the field is the strongest. The magnetic fields are in time quadrature with the electric fields, meaning that the magnetic field maximum occurs one-quarter period later in time than that of the electric field.

As mentioned above, the most commonly used mode in a DR is the $TE_{01\delta}$ mode, which is the lowest order mode. In this mode, the magnetic field resembles that of a magnetic dipole and is highly axial and homogeneous. The electric field forms concentric circles around the z-axis, is at a maximum at the periphery of the cylinder and is zero along the central axis where the magnetic field is the strongest. Consequently, a hole can be bored down the axis of the DR, for placement of an EPR or NMR sample, without appreciably disrupting the distribution of the fields, as shown in Figure 15, providing that the hole is not too large.

The field pattern of the $TE_{01\delta}$ mode is such that it can be excited with a small wire loop (or dipole) probe placed above, or to the side of, the DR. Alternatively the TE_{01} mode of a rectangular waveguide can be used as the excitation source, or a microstrip line placed near the resonator's circular end face. The orientation of any coupling mechanism should be such that the magnetic field lines link with those of the DR, as shown in Figure 16.

Resonant Frequencies of Dielectric Resonators

Although the exact frequency for a given resonant mode in a dielectric cylinder can only be calculated by rather complicated numerical procedures, an empirical estimation of the resonant frequency (f_r) of the $TE_{01\delta}$ mode of an isolated dielectric cylinder in free space is given by:

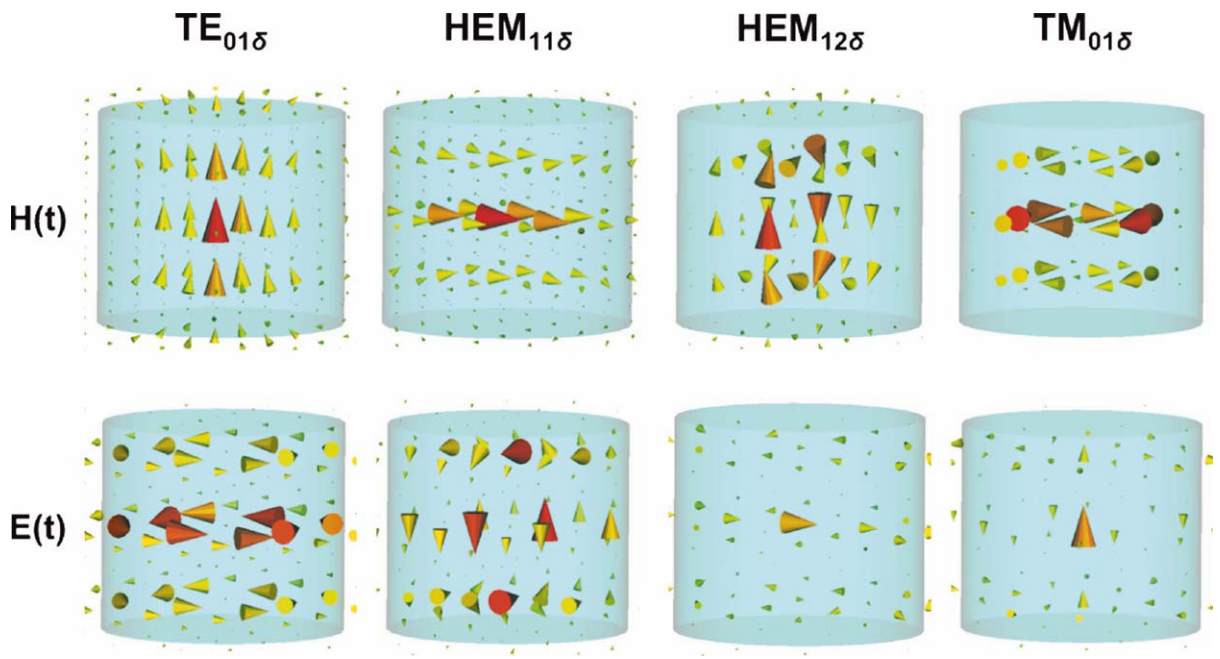

Figure 14 Electromagnetic simulations of the magnetic (top) and electric (bottom) field patterns at their peak values for the four lowest order modes of a cylindrical dielectric resonator: $TE_{01\delta}$, $HEM_{11\delta}$, $HEM_{12\delta}$, and $TM_{01\delta}$. The fields are strongest where the vectors (cones) are largest and darkest in color. Temporally, the $H(t)$ and $E(t)$ fields are 90° out of phase with each other.

$$f_r = \frac{3,400}{r\sqrt{\varepsilon_r}}\left(\frac{r}{h} + 3.45\right) \qquad [43]$$

where r is the radius, and h the height, of the cylinder in centimetres and f_r has units of MHz. This formula was originally derived (*6*) by fitting a straight line to the results of numerical solutions and is known to be accurate to about 2% in the range $0.5 < r/h < 2$ and $30 < \varepsilon_r < 50$. Although many DRs use materials with ε_r well above this range, the equation is a useful starting point in determining design parameters.

The shielding conditions also affect the resonant frequency (*7*, *8*). If a shield is placed around the circumference, or above and below the ends of the DR, then the resonant frequency is affected due to displacement of the electric and magnetic fields by the shield, and the direction of change of f_r can be determined from cavity perturbation theory (*9*). If the stored energy is mostly electric, moving a metal shielding wall closer to the resonator decreases the resonant frequency. Conversely, for a displaced field that is predominantly magnetic, the resonant

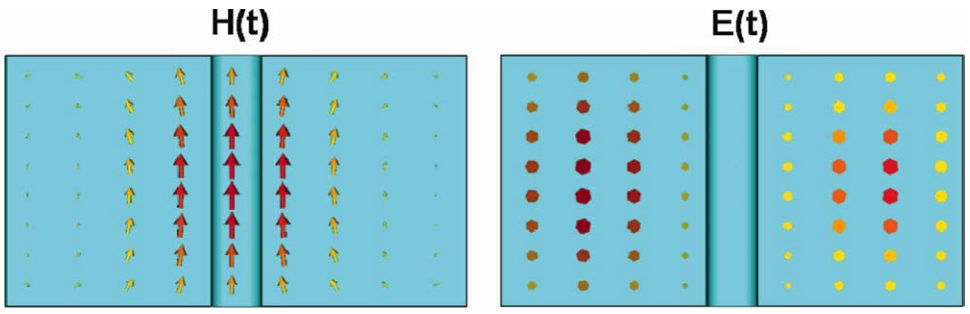

Figure 15 Magnetic (left) and electric (right) field distributions for the $TE_{01\delta}$ mode of a cylindrical dielectric resonator with a hollow bore. The magnetic field is highly axial and homogenous along the hollow bore. The electric field vectors are orthogonal to the plane of the page and are strongest at the periphery of the cylinder and zero within the hollow bore where the magnetic field is the strongest.

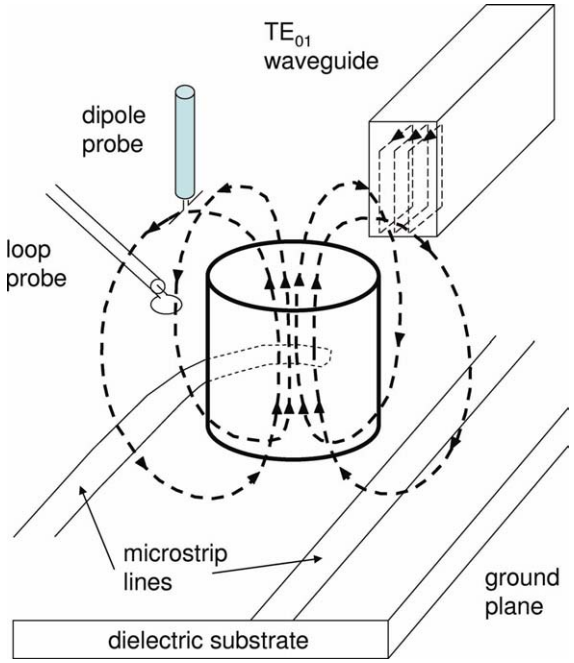

Figure 16 A schematic diagram of four different methods (microstrip, loop, dipole, and waveguide) of coupling energy into the DR, while also ideally providing an impedance match for maximum power transfer.

frequency increases. In the specific case of a DR operating in its $TE_{01\delta}$ mode, the frequency increases as a metal wall moves inwards towards the sides of the DR since the displaced energy is predominantly magnetic.

Knowledge of how shielding conditions affect the resonant frequency of a DR can be particularly useful when implementing tuning mechanisms. For the $TE_{01\delta}$ mode, bringing metal plates, or a tuning screw, closer to the circular surfaces of the DR will increase the resonant frequency, and vice-versa. One negative consequence of bringing a metal plate near the DR is that surface currents will be created, which reduce the Q value of the resonator. The unloaded quality factor, Q_u, of a DR is affected mainly by the dielectric losses in the DR itself (*10*) and so can be defined as:

$$Q_u = \frac{1}{\tan\delta} = \frac{\varepsilon'}{\varepsilon''} \qquad [44]$$

In general, ε' is relatively constant, and ε'' increases linearly with frequency, hence the Q_u of a dielectric resonator is inversely proportional to frequency. External losses can reduce the unloaded Q, and these losses include radiation, tuning mechanisms, adhesives used to support the resonators, and dissipation in the surrounding metal shield. It has been suggested that eddy currents in an outer shield become negligible for a shield 2–3 times larger in diameter than that of the resonator (*11*).

Temperature Stability

For MR experiments it is very important that the resonant frequency of the DR is constant during data acquisition to ensure maximum sensitivity. However, the properties of many dielectric materials are highly temperature dependent. The two major temperature-dependent effects in dielectric materials relate to thermal expansion of the material and an intrinsic variation in the permittivity itself.

Solids generally expand as a function of an increase in temperature. The linear coefficient of expansion (α_L) relates the change in a material's linear dimensions (ΔL) to a change in temperature (ΔT) by

$$\frac{\Delta L}{L} = \alpha_L \Delta T \qquad [45]$$

where L is the material's initial linear dimension. An increase in temperature produces an increase in L, the resonant wavelength of the DR therefore increases, and the resonant frequency decreases.

The relative permittivity of a material also varies with temperature. For most materials, over the limited range of temperatures relevant for MR operation, this effect is approximately linear:

$$\frac{\Delta\varepsilon_r}{\varepsilon_r} = \tau_\varepsilon \Delta T \qquad [46]$$

where τ_ε is the temperature coefficient of the permittivity, which can be either positive or negative depending upon the particular material. Since the resonant frequency is inversely proportional to $\sqrt{\varepsilon_r}$, a positive value of τ_ε results in a decrease in the resonant frequency. Hence, the resonant frequency of a DR changes as a function of temperature due to both linear expansion and the change in permittivity. The combined effect of both of these factors is called the temperature coefficient of the resonant frequency (τ_f). For the TE_{mn} or TM_{mn} modes of a DR the value of τ_f is given by:

$$\tau_f = -\alpha_L - \frac{1}{2}\tau_\varepsilon \qquad [47]$$

This equation is useful when to trying to achieve temperature compensation to minimize the temperature dependence of the resonance frequency of the

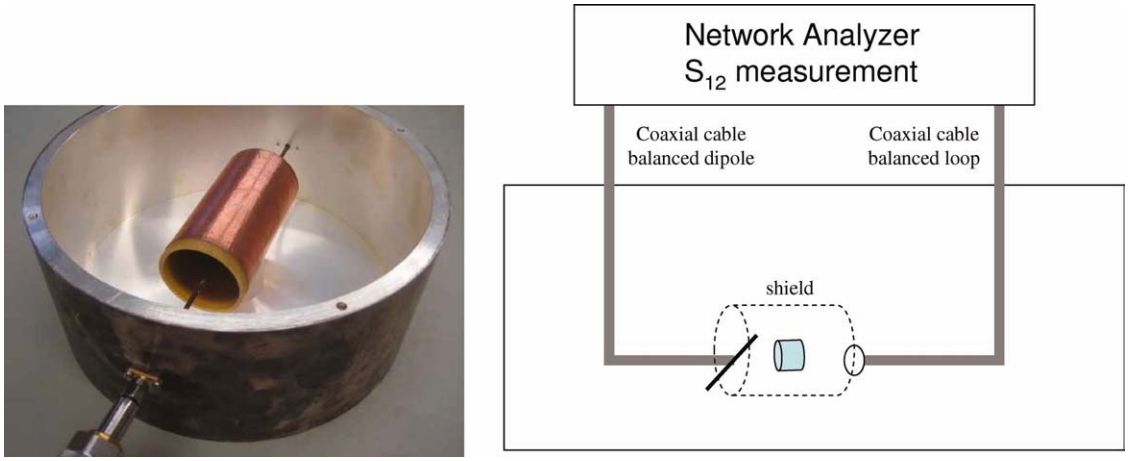

Figure 17 Setup for measuring the resonant frequency of a dielectric resonator via S-parameter methods using a standard two pickup-coil arrangement and copper shielding tube with identical dimensions to the RF shield used in the MR probe.

DR, either by modifying the composition or configuration. A temperature stable material needs to have a negative value of τ_ε given by:

$$\tau_\varepsilon = -2\alpha_L \qquad [48]$$

Commercial examples of such temperature compensated materials are those found in NP0 (negative-positive-zero) capacitors. These are used in a variety of high-power devices, including MR coils, and typically have a permittivity between 15 and 100, with a change of less than 0.4% in the permittivity over a temperature range of 55 to 125°C. These capacitors have a barium titanate content of between 15 and 50%, with calcium titanate, titanium dioxide, and traces of rare earth oxides such as samarium and neodynium added for temperature compensation. The grain size of the composite ceramic is ~1 μm, since the smaller the grain size the lower the temperature dependence. Values of τ_ε for specific dielectrics are given in Appendix A.

Dielectric Resonator Construction and Characterization

The typical starting material for a solid DR for EPR or MR applications is a dielectric such as $BaTiO_3$, $SrTiO_3$ or $CaTiO_3$ in powder form. This is moulded into a cylindrical shape using a die of the appropriate diameter. Forming uses both an axial press (at a pressure of ~15,000 psi) and a cold isostatic press (25,000 psi). The resulting green samples are then sintered in a furnace at 1,500°C for ~four hours. The powder typically has a lateral shrinkage of ~20% during sintering, and so the size must be made correspondingly larger than the final desired dimension, which is specified for a given resonance frequency from Eq. [43]. Once sintered, holes can be created in the ceramic discs using a diamond core drill. A diamond surface grinding wheel is used to achieve the final desired height, which is fine-tuned through experimental S_{21} measurements with a network analyzer using a standard two pickup-coil arrangement and a copper shielding tube identical to that used on the actual MR probe, with the assembly centered in a silver cavity as shown in Figure 17. The resonant frequency of the $TE_{01\delta}$ mode is divided by the -3 dB bandwidth to derive the *Q* value.

The resonant frequency of a DR can also be measured using methods that confine EM energy within the dielectric material. One of the most common methods is that of Hakki and Coleman (*12*) who used a dielectric resonant post bounded by two parallel conducting plates to measure the resonant frequency. Many other measurement methods are possible (*13–15*), although these are appropriate for very accurate measurements which are not typically required for MR applications.

Applications of Dielectric Resonators in EPR

This section comprises a short review of the use of DRs in EPR. The advantages of using DRs in EPR experiments have been well-documented and interested readers are pointed to a comprehensive review article (*16*).

The first use in EPR was by Carter and Okaya who discovered that a DR could be used to detect EPR signals of artificially produced boules of Fe^3 in rutile

(TiO_2, $\varepsilon_r \sim 100$) (*17*). The original rutile dielectric resonator was coincident with the Fe^{3+} sample, and paramagnetic resonances were observed over a range of 2-110 GHz in a field of up to 14 T. An increase in sensitivity was achieved by using the doped rutile as the microwave resonator rather than the traditional metal walled cavity, since rutile has a much higher loaded Q values ($\sim$5,000 for 50-110 GHz and $\sim$ 85,000 for 1.5-7 GHz all at 78 K) and the filling factor with the coincident sample was unity. An X-band comparison of the DR design with the traditional metal cavity resonator was made and showed the minimum number of detectable spins improved by a factor of 2,500 for the DR. Okaya (*18*) also noted that one of the big advantages of using the rutile resonator was its extremely small physical size when compared with traditional metal walled cavity resonators.

A dielectric cavity resonator (DCR) was demonstrated by Rosenbaum (*19*) and Harthoorn and Smidt (*20*). DCR configurations used either a hollow dielectric tube resonator with the sample inside, or a dielectric rod resonator as the (coincident) sample. Rosenbaum used teflon ($\varepsilon_r = 1.27$), quartz ($\varepsilon_r = 2.06$), lucalox ($\varepsilon_r = 9.9$), and ruby ($\varepsilon_r = 9.9$) as the dielectric materials operated at the X- and K_a-bands, achieving loaded Q-values as high as 5,000. Harthoorn and Smidt used fused silica ($\varepsilon_r = 3.8$) DCRs with inner radius 0.5 cm, outer radius 1.25 cm and length 1.156 cm resonating at 9 GHz in the TE_{011} mode with a measured unloaded Q of 6,300. Metal endplates were used on both sides of the DCRs.

Building upon Rosenbaum's work, Walsh and Rupp (*11*) presented the first systematic use of DRs in cylindrical configurations for use in EPR . They used resonators made from zirconium tin titanate (ε_r = 37.5) and barium titanate ($Ba_2Ti_9O_{20}$, $\varepsilon_r = 40$) to replace a conventional half-wavelength K_u–band waveguide cavity that had a resonant frequency at 11.6 GHz. In this case a single cylindrical disk was used in the TE_{011} mode. The center of the cylinder was drilled out to produce a hollow bore into which the sample could be placed. The center region of the cylinder could be removed for this operating mode with little change in frequency or field distribution,. In this case the use of a DR showed significant increases in signal-to-noise (S/N) (from $\sim$15$\times$ to $\sim$30$\times$ depending on the material) over the conventional waveguide cavity.

Dykstra and Markham (*21*) also investigated the use of DRs in EPR spectroscopy, using commercially available $(ZrSn)TiO_4$ dielectrics with $\varepsilon_r = 38$, $Q_0 =$ 5,300 at 8.8 GHz, height = 2.65 mm, outer diameter = 5.98 mm, and a temperature stability of less than 2 ppm/°C. Holes of diameter 1 mm and 2 mm were created within the DR to insert the sample tubes, and the corresponding operating frequencies were then 8.85 GHz and 8.91 GHz respectively. For small samples the sensitivity increased by two orders of magnitude for the DR when compared to a standard cavity.

A dual disk arrangement was presented in 1992 by Bromberg and Chan (*22*) who designed a coupled two-disk TiO_2 system for EPR studies using a modified diamond anvil cell (DAC). The resonant frequency was 11.2 GHz at 77 K and 9.5 GHz at 2 K when the disks were in the $TE_{01\delta}$ mode. A typical loaded Q was $\sim$1,200 at room temperature and 5,000 at 2 K. Substantial improvements in Q and filling factor were noted from Sakai's original design of a conventional DAC for EPR in the X-band (*23*).

Sienkiewicz and Qu (*24*) used both single and double disk structures for stopped-flow EPR experiments in the X-band (9.05 – 10 GHz). Their zirconium titanate ($\varepsilon_r = 30$) disks were also hollow and tuned to resonate at various frequencies of the $TE_{01\delta}$ mode by changing the spacing between the double disks. Lassmann et al. (*25*) also used a zirconium titanate ($\varepsilon_r = 30$) double disk arrangement to perform EPR stopped-flow experiments in the X-band.

Since there are no closed-form analytical solutions to determine the exact resonant frequency of cylindrical dielectric resonators in free space, Jaworski et al. (*9*) derived an approximate method for predicting the resonant frequencies for single and stacked dielectric resonators used in sensitive EPR measurements. Jaworski first studied single and double-stacked dielectric configurations, which were designed using commercially available X-band high-dielectric ceramics. Their configuration was very similar to that of Sienkiewicz (*24*) in that a microwave shield was used as well as a laterally protruded loop-shaped antenna for magnetic coupling to the $TE_{01\delta}$ mode. Jaworski et al. developed a semi-empirical model to bridge the gap between these two approaches. The model employed a combination of approximate analytical formulae with their experimental results for both single and double-stacked resonator structures. Their approach yielded accuracy better than one percent for the commercial DRs. Furthermore, when comparing the single DR to the double DR, it was noted that a higher filling factor could be obtained for a point sample in the single DR structure, but the double-stacked configuration yielded better SNR for long aqueous samples, as shown in Figure 18.

Dielectric Resonators in Human MRI

The concept of a DR can be adapted for human MRI. The resonators are necessarily much larger in size

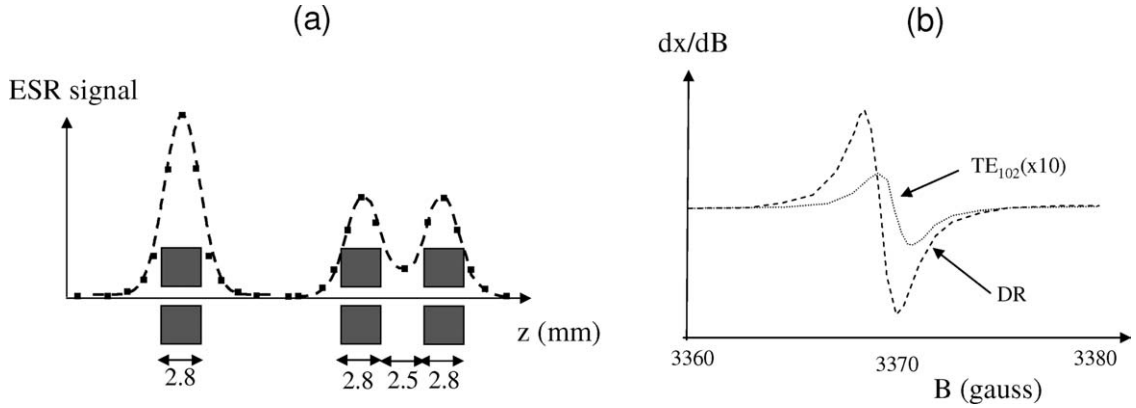

Figure 18 (a) A comparison of the relative estimated and measured EPR line intensities as a function of the point-DPPH sample position. On the far left the relative EPR signal intensity for the point sample probing H_z^2 along the z axis of the single DR. Adjacent is the relative EPR signal intensity along the z-axis of the double-stacked DR. The solid squares represent experimental results and the solid line the estimated signal. (b) EPR spectra of TE point-DPPH sample measured in a double-stacked DR structure and in a standard TE_{102} cavity. The spectra were recorded with the same incident microwave power (0.2 mW) and with the same effective magnetic field modulation (0.5 G). Figure adapted from reference (*9*).

and are resonant at much lower frequencies than for EPR. Wen et al. (*26*) constructed a series of cylindrical and annular dielectric resonators that used either water or D_2O as the dielectric for a whole-body 4 T (170.75 MHz) MRI system. Using a complete cylinder of water of diameter 24.8 cm, they measured the frequencies of the first three modes using cylinder lengths of 6.5 cm ($TE_{01\delta}$, ~100 MHz), 12.1 cm ($HEM_{11\delta}$, ~170 MHz) and 25 cm (a tilted $TM_{01\delta}$ mode ~280 MHz). They also showed that a cylinder of water with an outer diameter 19 cm, inner diameter 8 cm, and height 16.9 cm gave a $TE_{01\delta}$ resonance at ~170 MHz. Coupling to the DRs in this case was via an inductive loop and a matching circuit placed above the resonator. The $TE_{01\delta}$ mode was utilized, and the object to be imaged was placed into a cylinder containing water or D_2O. This study was successful in obtaining an image of a hand, but the authors noted that the high-loss factor of water does not make it an ideal dielectric, in addition to the fact that the sample becomes "undesirably wet"! The authors also noted that if the coil is to be used as a head or body resonator, then the HEM mode must be used since it produces a (quadrature) field perpendicular to the main magnetic field, B_0.

Dielectric Resonators in Magnetic Resonance Microscopy

The higher frequencies (400–900 MHz) used for MR microscopy in combination with the small diameter of, in particular, vertical bore systems means that high permittivity materials need to be used. The use of high permittivity dielectrics for high field MR microimaging was first shown by Neuberger et al. (*27*) at 14.1 T (600 MHz). The ceramic material used was barium strontium titanate ($Ba_{0.04}Sr_{0.96}TiO_3$), which has a very high relative permittivity of 323, but is relatively difficult to machine. Due to this and other manufacturing constraints, a solid (as opposed to hollow) double-stacked arrangement was used, with the sample placed between the two discs. The resonant frequency of the two disks, each of diameter 28.5 mm and height 12.2 mm, was fine-tuned with copper "paddles," as shown in Figure 19(a). The magnetic field was coupled into the resonators using a transmit/receive loop probe placed between the discs. The simulated EM fields shown in Figure 19(b) illustrate that there is a small dip in the magnetic field between the two resonators, and that the electric field is zero at the centre of the resonator, as expected. While Neuberger's resonator setup is not the optimal geometry in terms of available sample space or B_1 homogeneity, the configuration achieved significantly higher S/N when compared to a conventional saddle coil of similar dimensions. Example images from the DR are shown in Figure 19(c).

An alternative material for a DR is $CaTiO_3$, ε_r value 156, which is much more easy to machine, and is widely available at reasonable cost (<$100 per RF coil). By drilling a hole through the center of the cylindrical resonator (Fig. 15) the magnetic field distribution of the resonator is used more efficiently than the Neuberger design and larger samples up to

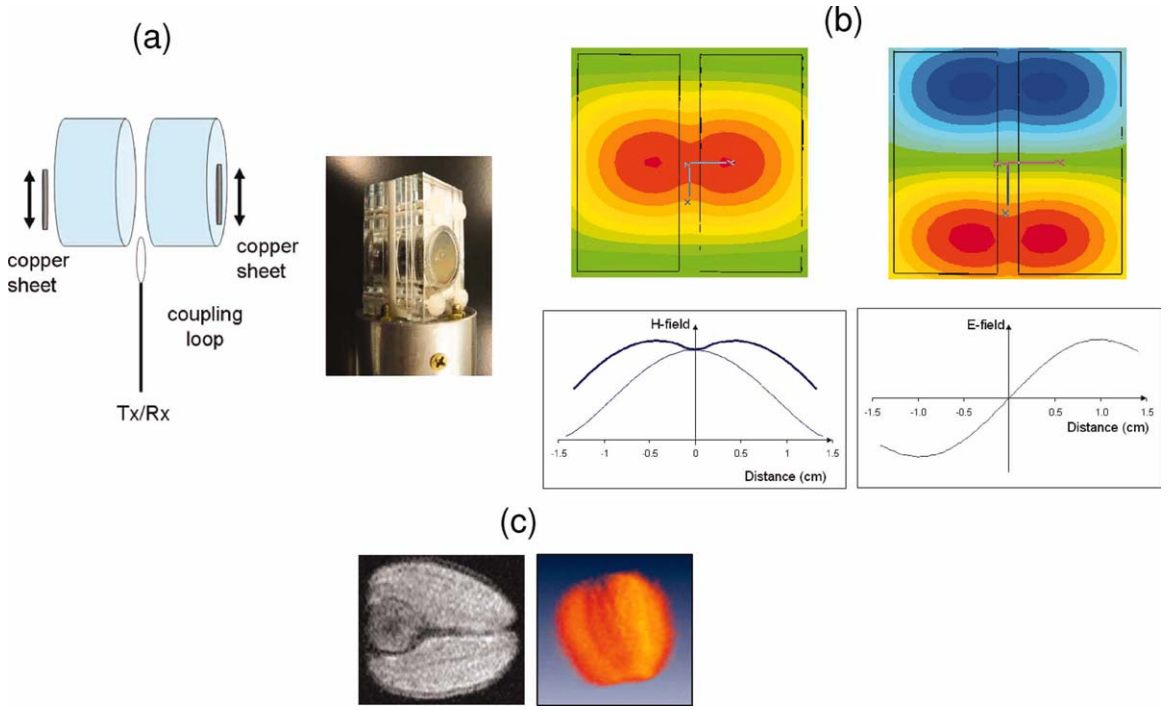

Figure 19 (a) Schematic and photographs of split cylinder barium strontium titanate DR operating at 600 MHz. (b) plots of the magnetic field and electric fields produced by the split resonator fed by a small loop coil. (c) One slice of a three-dimensional data set from a spin-echo imaging sequence of the lipid signal in a canola seed using the dielectric resonator. 192 × 192 × 140 data matrix, spatial resolution 20 × 20 × 30 μm, TR 1s, TE 10 ms, 4 averages. Also shown is the three-dimensional surface plot of the seed.

4.5 mm in diameter could be investigated (*28*). The efficiency of the DR was quantified by measuring a B_1 per square root of power of 294 $\mu T/\sqrt{Watts}$. For comparison, a loop gap resonator was constructed with equal length and inner diameter to the DR. The pulse width for this RF coil was ~25% larger than for the DR, indicating a higher sensitivity for the DR. MR microscopy experiments were performed on an ex vivo six week old zebrafish. After euthanizing the fish, it was fixed in a 4% formalin solution for 24 hours. Before imaging, the fish was placed into a phosphate buffered saline (PBS) with a 2% v/v Gd-DPTA (Magnevist) solution for two days to shorten the T_1 relaxation time: sodium azide was added as a biocide. The fish was then placed inside a 4 mm diameter glass tube of length 2 cm and filled with a perfluorinated liquid for the imaging experiment. The tube was centered within the DR, and a 3D spin-echo sequence (TR/TE 250/20 ms, spatial resolution 47 × 42 × 42 μm, four signal averages, total scan time 1 hour) was performed. Higher spatial resolution (20 × 20 × 25 μm) experiments were also performed, using 12 averages and took 16 hours to acquire. Representative images are shown in Figure 20.

The highest frequency at which DRs have been designed for MR is 900 MHz on the wide bore spectrometer at the National High Magnetic Field Laboratory in Tallahassee, Florida. The probe was constructed from $CaTiO_3$, with the following parameters: measured $\varepsilon_r = 166$ (a different commercial source to the previously described resonator), height = 1.43 cm, radius = 1.5 cm, and hole diameter = 4.8 mm. The cylindrical DR was enclosed within a copper shield of diameter 3.8 cm to fit snugly within the gradient set. In simulations this configuration gave a $TE_{01\delta}$ mode resonance at 874.8 MHz. The frequency was tuned to 900 MHz using copper paddles as described previously. Figure 21 shows the resonator, a measured transmit RF (B_1^+) field map along the axis of the hole, and images from excised rat spinal cord and muscle tissue.

With the trend towards ever-increasing magnetic field strengths, and concrete plans from at least two facilities to design MR magnets at 1.3 GHz by incorporating high-temperature superconducting inserts into standard magnet designs, the use of DRs is a very promising approach for constructing RF probes for such systems. At higher frequencies the dimensions of the DR become smaller, the very sim-

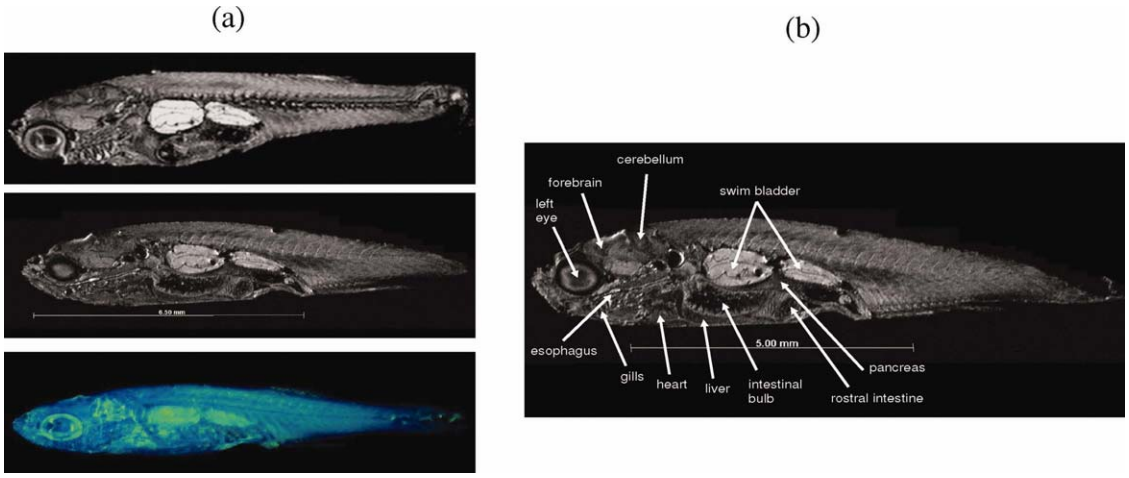

Figure 20 (a) (top) Single slice from a 3D data set of a fixed zebrafish acquired at a spatial resolution of 47 × 42 × 42 μm. (middle) Single slice from a 3D data set acquired at a spatial resolution of 25 × 20 × 20 μm. (bottom) Full 3D high resolution data set, volume rendered. (b) Detailed mapping of structures and organs based upon the images acquired at a resolution of 25 × 20 × 20 μm.

ple construction obviates the need for extensive lumped elements, there are no skin effects (such as occur in conductors), and the NMR environment typically provides very tight temperature control for highly stable operating conditions.

6. USE OF DIELECTRIC INSERTS FOR INCREASED SENSITIVITY AND REDUCED SAMPLE HEATING

An alternative use of dielectric materials is to incorporate them into the structure of a conventional resonator such as a birdcage or TEM coil. There are three basic possibilities:

i. the dielectric can be placed between the RF coil and the RF shield surrounding the coil to increase the radial RF homogeneity,
ii. the dielectric can be used as a "circular" liner to the RF coil to increase the sensitivity and/or shield the sample from the conservative electric field of the RF coil, or
iii. the dielectric can be selectively placed around different parts of the sample to

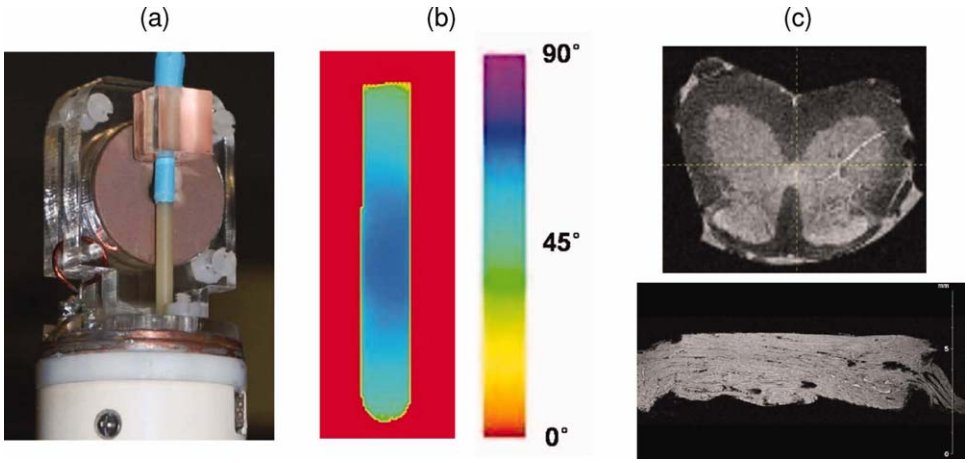

Figure 21 (a) Photograph of the calcium titanate DR probehead for operation at 900 MHz (without the shielding tube). (b) Measured distribution of tip angles along the length of the resonator. (c) top: excised amyotrophic lateral sclerosis (ALS) mouse spinal cord at 25 μm isotropic resolution, bottom: Excised rat soleus muscle at isotropic 20 μm resolution.

increase the RF sensitivity in areas of low transmission/reception efficiency.

Each of these possibilities have been explored by different groups, and each represents a promising solution to some intrinsic problems of very high frequency magnetic resonance. These three ideas are summarized below.

Increasing the Radial RF Homogeneity at High Field

For the first case mentioned above, Foo et al. (*29*) placed high dielectric material between the rungs and shield of a high-pass birdcage coil, with experiments and simulations performed at 170 MHz (4 T). At high field, due to the high permittivity of the body (*30–32*), the wavelength of EM energy in the body is shortened considerably compared to that in free space, Eq. [36], and areas of significant constructive and destructive interference occur in the body at field strengths above ~3 T. The authors showed that these sample-induced radial (*x,y*) field inhomogeneities could be reduced by using dielectric material placed between the RF coil and shield, although they also showed the trade-offs in terms of the power required for a certain B_1 field at the centre of the sample being increased, and the axial (*z*-direction) B_1 homogeneity being decreased substantially. For a high-pass birdcage, the current density $\boldsymbol{J}(\phi,z)$ is a function of the RF propagation constant, k_z, in the z-direction:

$$\vec{J}(\phi, z) = J_0 \sin\phi e^{-jk_z z}\hat{z} \qquad [49]$$

where ϕ is the azimuthal angle measured tangentially to the axial direction, and k_z is the axial wavenumber given by:

$$k_z = \frac{2\pi}{\lambda_z} \qquad [50]$$

At low field, k_z can be assumed to be zero, with no subsequent phase variation along the length of the rungs of the birdcage, and the current density is simply given by $J_0 \sin\phi$. However, this is not true at high field where significant phase variations can occur along the length of the birdcage rungs.

In terms of the magnetic, dielectric and conductivity properties of tissue, the propagation constant (k) in the body is given by:

$$k^2 = \omega^2\mu\varepsilon_0\varepsilon_r - j\omega\mu\sigma \qquad [51]$$

The RF field amplitude distribution in the radial plane is characterized by a corresponding radial propagation constant, k_ρ (*33*), and the relationship between the respective propagation constants is given by:

$$k_\rho^2 = k^2 - k_z^2 \qquad [52]$$

One way to increase the B_1 homogeneity in the radial direction is to effectively increase the "radial wavelength," λ_ρ, given by:

$$\lambda_\rho = \frac{2\pi}{k_\rho} \qquad [53]$$

From the equations above, minimizing the value of k_ρ can be achieved by increasing k_z, which in turn can be realized by loading materials of high permittivity into the coil-to-shield space. For simulations of a body coil at 64 MHz, which corresponds to a coil of head-sized proportions at 170 MHz (4 T), the authors found an optimal value of the permittivity of ~40, which represents a trade-off between reducing the radial RF inhomogeneity while maintaining acceptable axial homogeneity. If the value of k_z becomes too high then there are significant nulls in the current as it travels along the length of the conductor and the axial homogeneity deteriorates significantly. Figure 22 shows representative results from their simulations, which were confirmed by experimental measurements in phantoms.

Increasing the Sensitivity by Filling the Resonator

In an alternative approach, Butterworth et al. (*34*) filled a toroidal RF coil with high permittivity TiO_2. Titanium dioxide exists in three different crystalline forms (rutile, anatase and brookite) at room temperature. The rutile structure consists of chains of trans edge-sharing TiO_6 octahedra where the chains are connected by sharing corners, as shown in Figure 2(c). The toroidal cavity was designed to operate in the TEM_{00} (cyclotron) mode at 4.1 T. The authors measured S/N improvements of up to a factor-of-three for the filled vs. empty coil, and attributed this effect to minimization of the dielectric mismatch between air and the sample.

Reduced Sample Heating and Increased Sensitivity Using Dielectric Sleeves

There are a number of MR experiments which require very high RF power. These occur particularly in solid state NMR, but also include high power proton decoupling in liquid samples. If the sample has a

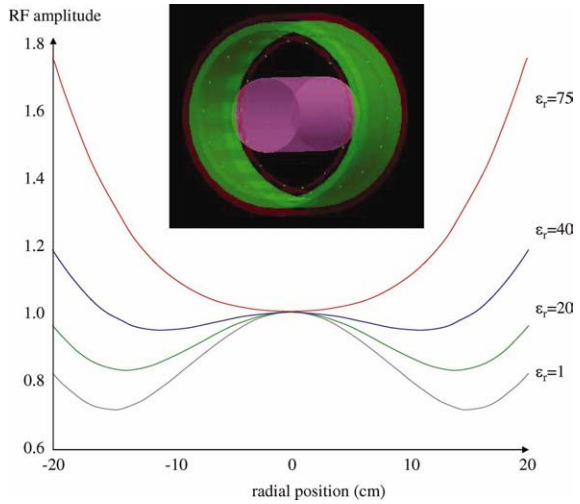

Figure 22 Radial field amplitude profiles for different permittivity materials placed between the RF coil and shield for a full-sized body coil at 64 MHz. A homogeneous phantom was placed symmetrically within the coil.

high conductivity (such as biological samples containing a significant salt content) then the sample can undergo significant heating due to the electric fields produced by the RF coil. The coil geometry with the highest intrinsic S/N, the solenoid shown in Figure 23(a), is particularly problematic in that it produces a very high electric field at the centre of the sample, as shown in Figure 23(c). Although other types of coil with lower E-fields can be used, such as modified Alderman-Grant designs (*35–38*) or scroll-coils (*39*), these geometries typically have a lower S/N than the solenoid. Crum and Zilm (*40*) have suggested that it should be possible to shield the sample from the conservative component of the electric fields that are produced by a solenoid, without significantly altering either the B_1 field distribution or amplitude, by the use of a cylindrical dielectric sleeve which is placed between the sample and coil as shown in Figure 23(b). EM simulations presented in Figure 23 shows that this is indeed the case. The reduction of the conservative E field in Figure 23(d) with the dielectric shield in place, compared to the situation in Figure 23(c) with no shield, is quite substantial. Also Figures 23(e,f) show that the shield has very little effect on the magnetic field distribution within the sample.

This concept has been further developed by Neufeld et al. (*41*) who inserted a dielectric cylinder of deuterated water into a high field NMR probe. They measured a S/N increase of ~20% compared to

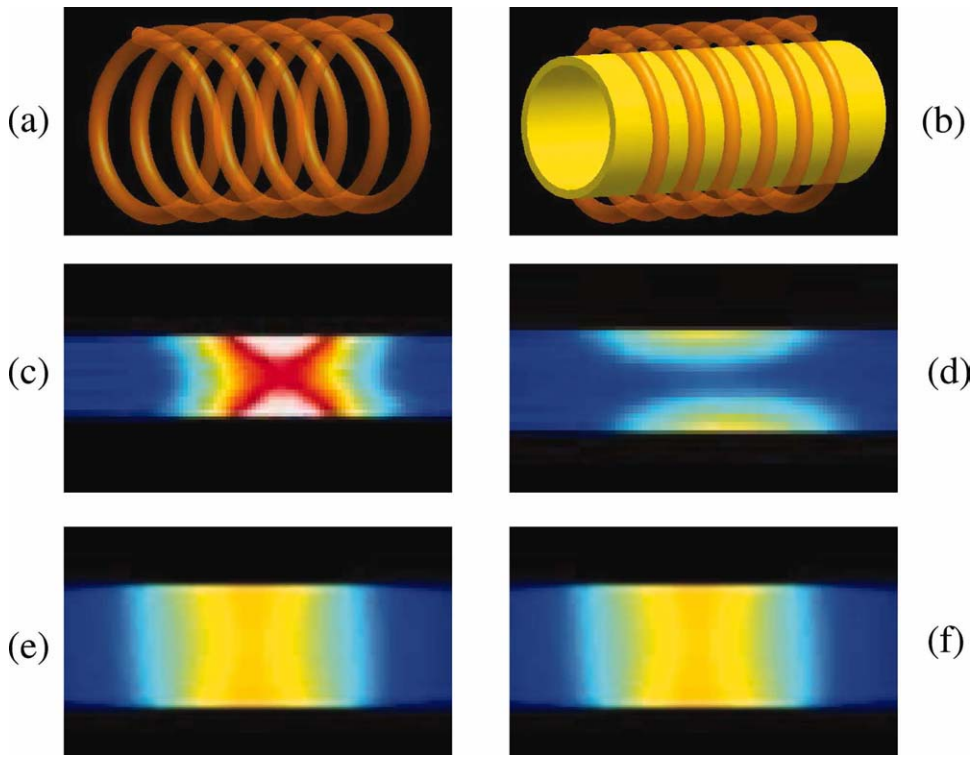

Figure 23 Electromagnetic simulations showing the effect of a dielectric shield (yellow) on the conservative electric fields, (c) and (d), and the magnetic field, (e) and (f), when placed inside a solenoidal coil (a). The magnitude of the conservative electric field is reduced substantially.

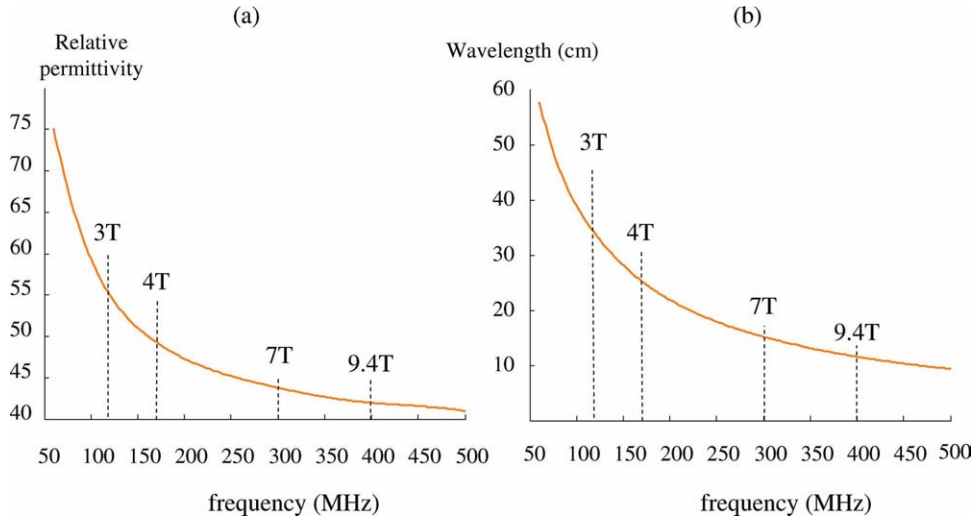

Figure 24 (a) The relative permittivity of muscle as a function of frequency. (b) The wavelength of EM energy in muscle decreases roughly exponentially as a function of frequency.

having an equivalently-sized empty cylinder. One disadvantage of this approach, as they noted, is that a relatively thick dielectric cylinder was required, which reduces the filling factor of the NMR probe considerably. This constitutes a good reason for further investigation of very high dielectric materials, which could be made much thinner, thus increasing the filling factor and futher enhancing the S/N.

7. USE OF HIGH PERMITTIVITY PADS FOR HUMAN MRI

It is often stated in medical imaging textbooks that MRI "does not suffer from penetration effects" unlike other imaging techniques such as, for example, ultrasonic imaging. However, this statement is only true if the wavelength of the RF within tissue is much greater than the dimensions of the body part being imaged. Although Figure 24(a) shows that the relative permittivity of tissue, in this case muscle, decreases with frequency, this is an effect which tails off at fields above 4 T, and so there is a significant decrease in the EM wavelength at high field, as shown in Figure 24(b). The RF wavelengths at 1.5, 3, 7, and 9.4 T are ~55, 30, 14, and 10 cm, respectively. Similar values are found for tissues such as white and gray matter in the brain (*30–32*).

Using a standard RF coil the short wavelength (relative to the body's dimensions) can create a "standing wave" pattern with constructive interference near the center of the sample and regions of destructive interference at a distance of approximately one quarter-wavelength from the coil. An example of this is shown in Figure 25, which simulates gradient echo images at various field strengths (*42*). The effect of the B_1^+ inhomogeneity as field strength increases has been studied extensively by many research groups (*43–46*).

In addition to the problems of producing a homogeneous transmit field, the second major challenge in high field MRI is the heating produced by the electric field within the body (*47*, *48*). Basic electromagnetics shows that there must be an RF electric field associated with any RF magnetic field, and this electric field produces electrical currents in conductive tissues. The power deposited in the body can be calculated very simply in terms of the specific absorption rate (SAR) given in Watts per kilogram of tissue.

$$\mathrm{SAR} = \frac{\sigma}{2\rho}|E|^2 \qquad [54]$$

where σ is the tissue conductivity and ρ is the material density. There are strict regulatory guidelines on these values (*49*) in terms of peak instantaneous and time-averaged values for both local and global regions-of-interest.

Many research groups have shown that the use of transmit arrays, with the magnitude and phase of the driving signal inputs to each element of the array being independently controllable, can increase the RF homogeneity at 7 T (*50*) and 9.4 T (*51*). This approach has shown improvements both in terms of image uniformity and reduced power deposition, but it does increase the complexity of the MR system significantly, requires complicated monitoring to ensure that localized areas of tissue heating are not

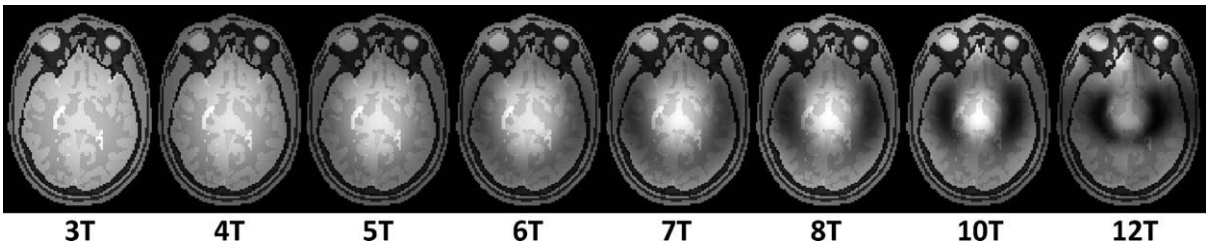

Figure 25 Simulated gradient-echo images, assuming a low tip-angle excitation, as a function of field strength using a birdcage coil with ideal current distributions in the rungs.

produced, and currently is not used in a routine clinical environment. The use of specialized RF pulses (*52*) to mitigate RF inhomogeneity is also an area of active research, but requires significant changes to scanning protocols. A more simple approach to improving the homogeneity of the transmit field, outlined in the following sections, is to use judiciously-placed high permittivity materials to alter the spatial distribution of the RF fields within the body.

Applications of Water-Based Dielectric Pads at Clinical MRI Field Strengths

Even at clinical fields of 3 T, significant areas of signal nonuniformity are evident when imaging the abdominal area of certain patients, as shown in Figure 26(a). The use of very simple aqueous gel-based dielectric bags has been suggested for 3 T imaging (*53–56*) as a way to reduce the dark areas on turbo spin-echo T_2-weighted sequences, which are part of standard imaging protocols. For example, Sreenivas (*54*) used 4-L bags filled with water, which were doped with between 20 and 50 mM manganese salts to reduce the background MR signal. Similar work has been reported in phantoms by Takayama et al. (*55*) and Sunaga et al. (*56*), who designed a gel with permittivity similar to tissue for improved impedance matching to human skin. Figure 26(b) shows an example of the improvements in image quality possible using this approach.

There are two mechanisms by which this approach works. First, it is well-known that the more elliptical the structure the more spatially inhomogeneous the RF field produced by the quadrature body RF coil, which is usually a cylindrical birdcage (*57*). Addition of a dielectric pad on the abdomen effectively reduces the elliptical eccentricity of the patient, therefore "improving" the geometry. Second, displacement currents within the pad create a secondary magnetic field which can add to the primary field from the RF coil: this is discussed further in "Applications of Dielectric Suspensions to High Field MRI" section. In Figure 26(b) the dielectric pad (invisible in the image) was placed on top of the abdomen, and the secondary magnetic field "fills in" the void in the image shown in Figure 26(a). The concept of aqueous dielectrics has been extended by Yang et al. (*58*) who have surrounded the head with a pad containing water and performed both simulations and experimental imaging at 3 T. The setup and represen-

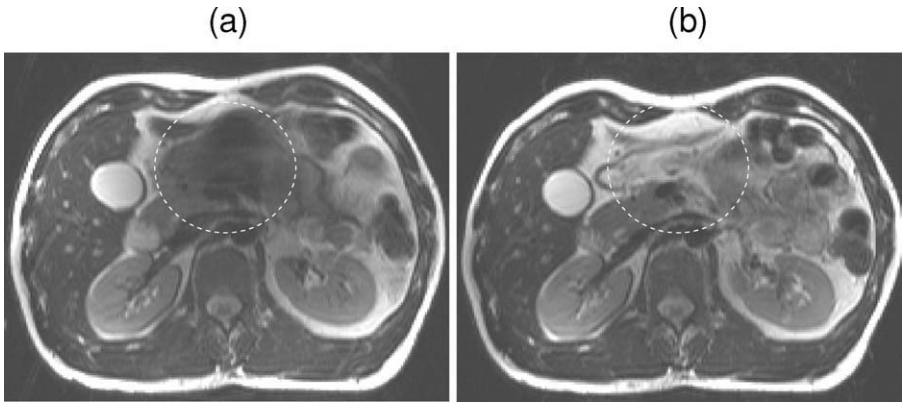

Figure 26 Abdominal images, (a) acquired using a standard TSE clinical sequence at 3 T. Severe shading is seen in the outlined region, and (b) by placing a dielectric pad made of ultrasound gel and doped with paramagnetic contrast agent on top of the patient, the homogeneity of the image increases significantly. Images reproduced from (*53*).

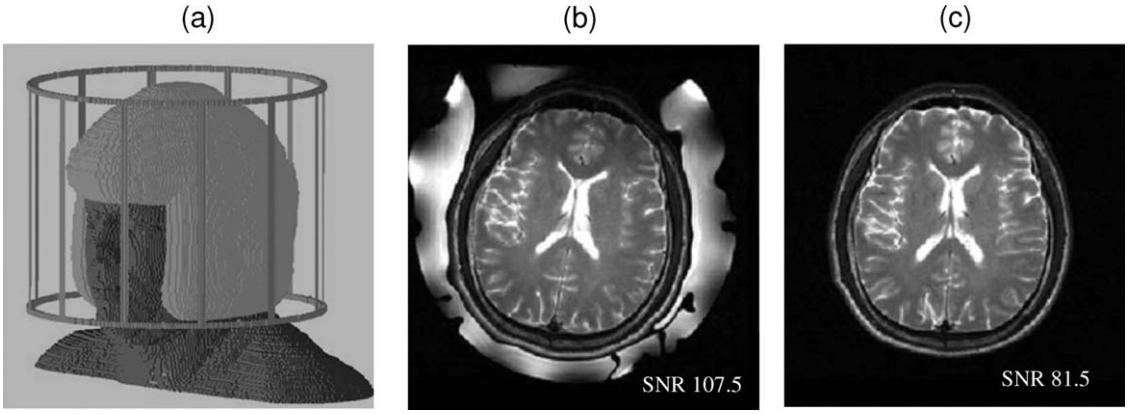

Figure 27 (a) Computer model of a birdcage coil, human head, and water padding around the head. Axial images through the brain, with (b) and without (c) the water padding, with measured S/N over the whole slice.

tative images are shown in Figure 27. The authors find significantly increased S/N measured over the whole brain, and point out that this in turn leads to a decreased SAR since the input power necessary to reach a certain flip angle is reduced. The only disadvantage of this approach is the fact that a large space is required for the relatively thick water bag, and this reduces the filling factor. In practice a close-fitting phased array receiver would be used, and so again the use of high dielectric materials might be anticipated to improve this situation by being able to use much thinner pads. The next section describes how different liquids and liquids/solids can be mixed to give permittivities of specified values.

Mixing Rules for Dielectrics

In many cases, the optimum permittivity required for a particular application may not correspond to a material with appropriate physical properties. For example, there is no liquid with a permittivity of ~60 which could be used for (bio)medical applications. The obvious solution is to mix different liquids, or alternatively liquids and solids to form a suspension, to obtain the desired value of ε_r. This section summarizes some of the very simple mixing rules used to predict the value of ε_r of mixtures or suspensions, or to estimate the composition to produce a desired value of ε_r.

Mixing Rules for Liquids. By varying the proportions of miscible liquids with high and low permittivities, a continuum of values can be produced. For MR applications any background MR signal can be reduced significantly either by using deuterated solvents, or alternatively by dissolving paramagnetic or ferromagnetic compounds to reduce the T_2 value of protonated solvents,.

When liquids are mixed, it should be noted that there can be signifcant changes in volume and also quite complicated orientational correlations between different (particularly polar) species. However, one usually assumes that the polarization for each component does not change when mixed, in which case the effective dielectric constant (ε_{eff}) of the mixture is simply given by:

$$\varepsilon_{eff} = \varepsilon_0 \alpha \vec{p}_{mixture} = \varepsilon_0 \rho_{mixture} \sum_{i=1}^{n} \alpha_i x_i v_i \vec{p}_i \qquad [55]$$

where x_i is the mole fraction, v_i is the molar volume, $\mathbf{p}_i$ the polarization of species i, n the total number of components, and ρ the density. Equation [55] is known as Oster's rule (*59*). Assuming zero volume change, this can be simplified to:

$$\varepsilon_{eff} = \varepsilon_0 \sum_{i=1}^{n} \alpha_i \Phi_i p_i \qquad [56]$$

where Φ_i is the volume fraction based on the molar volumes of the pure components:

$$\Phi_i = \frac{x_i v_i}{\sum_{k=1}^{n} x_k v_k} \qquad [57]$$

For an extensive discussion of estimating the permittivity of fluid mixtures at different temperatures and pressures, see Harvey and Prausnitz (*60*).

Mixing Rules for Suspensions. As described in the next section, the use of deuterated suspensions of metal titanates shows great promise for improving the RF homogeneity in human imaging at 7 T and above. The concept of an effective macroscopic per-

mittivity of a suspension implies that the suspension responds to EM excitation as if it were homogeneous. This effectively constitutes a "quasi-static approach" (similar to modeling the magnetic fields from RF coils assuming no wavelength effects), and can be used providing that the size of any particle is below approximately one-tenth of the EM wavelength. If the density of the particles (termed inclusions) is high it is important to analyze how their dipole moments "communicate" with each other.

There are many laws which describe the behavior of a mixture or composite of two different dielectric materials. The classical theoretical models are based upon calculating the polarizability of a single sphere of dielectric material, which is given by:

$$\alpha = V(\varepsilon_i - \varepsilon_e)\frac{3\varepsilon_e}{\varepsilon_i + 2\varepsilon_e} \qquad [58]$$

where V is the volume of the sphere, ε_i is the permittivity of the inclusions (e.g., metal titanate particles), and ε_e that of the surrounding environment (e.g., deuterated water). In this case the effective permittivity is given by the Clausius-Mossotti formula (also referred to as the Lorenz-Lorentz formula):

$$\varepsilon_{\text{eff}} = \varepsilon_e + \frac{n\alpha}{1 - n\alpha/3\varepsilon_e} \qquad [59]$$

where n is the number density of dipole moments. These two equations can be combined to give the Maxwell Garnett formula:

$$\varepsilon_{\text{eff}} = \varepsilon_e + 3f\varepsilon_e\frac{\varepsilon_i - \varepsilon_e}{\varepsilon_i + 2\varepsilon_e - f(\varepsilon_i - \varepsilon_e)} \qquad [60]$$

where f is the fraction of inclusions. In the limits, when $f \to 0$ then $\varepsilon_{\text{eff}} \to \varepsilon_e$, and when $f \to 1$ then $\varepsilon_{\text{eff}} \to \varepsilon_i$, as expected. There are a large number of related models, including the Bruggeman/Polder-van Santen and the "Unified mixing formula," which are covered in detail in reference (*61*).

A set of very useful and simple semiempirical [although it should be noted that a recent publication provides a rigorous derivation of these laws from Maxwell's equations (62)] dielectric mixing laws are knows as Lichtenecker's equations (63). One example is Lichtenecker's power law, which is given by:

$$\varepsilon_{\text{eff}}^{\sigma} = f_1\varepsilon_1^{\sigma} + f_2\varepsilon_2^{\sigma} \qquad [61]$$

where the coefficient σ lies between -1 and 1. Specific values of σ correspond to well-known equations, for example $\sigma = 1/3$ to the Looyenga equation and $\sigma = ½$ to the Krawzenski equations, with $\sigma = 1$ representing a linear law. Another very simple law is Lichtenecker's logarithmic law:

$$\log(\varepsilon_{\text{eff}}) = \sum_{i=1}^{m} v_i \log \varepsilon_i \qquad [62]$$

There are also a number of more sophisticated models which take into account the fact that the interface between the two phases can play a critical role. For example, the Vo-Shi model (*64*) can be used for cases in which the formation of interfacial dipoles with high molecular polarizability occurs (*65–67*). For an extensive review of the mixing rule development see Sihvola (*61*).

In section 7 it is shown that simple suspensions follow Lichtenecker's power law well, but that addition of chemical dispersants, to increase the maximum concentration of high permeability materials before the mixture saturates, causes significant deviations from this behavior. In this case, a more complicated model such as the Vo-Shi may be necessary for accurate modeling.

Applications of Dielectric Suspensions to High Field MRI

The gel-based commercial dielectric pads in current use at 3 T are relatively thick in size (several cm), rigid and heavy. They have a relative permittivity of ~60, and since they contain significant paramagnetic concentrations, can cause signal loss in single-shot rapid imaging or long echo-time gradient-echo sequences due to strong magnetic susceptibility effects. Particularly for studies at high magnetic fields, one would ideally like a material which has a permittivity higher than water (but which also offers the possibility to be tailored in value), a low background MR signal without paramagnetic doping, and one which can be geometrically formed to adapt to different patient sizes.

One possibility is to use the calcium and barium titanates already outlined in the section on dielectric resonators. Although these materials have a very high permittivity when they are sintered and pressed, the values for the native powders are much lower, since the volume ratio of the powder is only ~40%, i.e., 60% of the volume of a given sample is air. However, by creating a suspension of the powders with deionized water, the permittivity can be increased, with a value that can be tailored by the appropriate composition of the suspension. These powders are widely availability at low cost. The properties of these suspensions, as expanded in later sections, are: (i) a high permittivity between 100 and 120 for calcium titanate and 150–250 for barium titanate, (ii) a

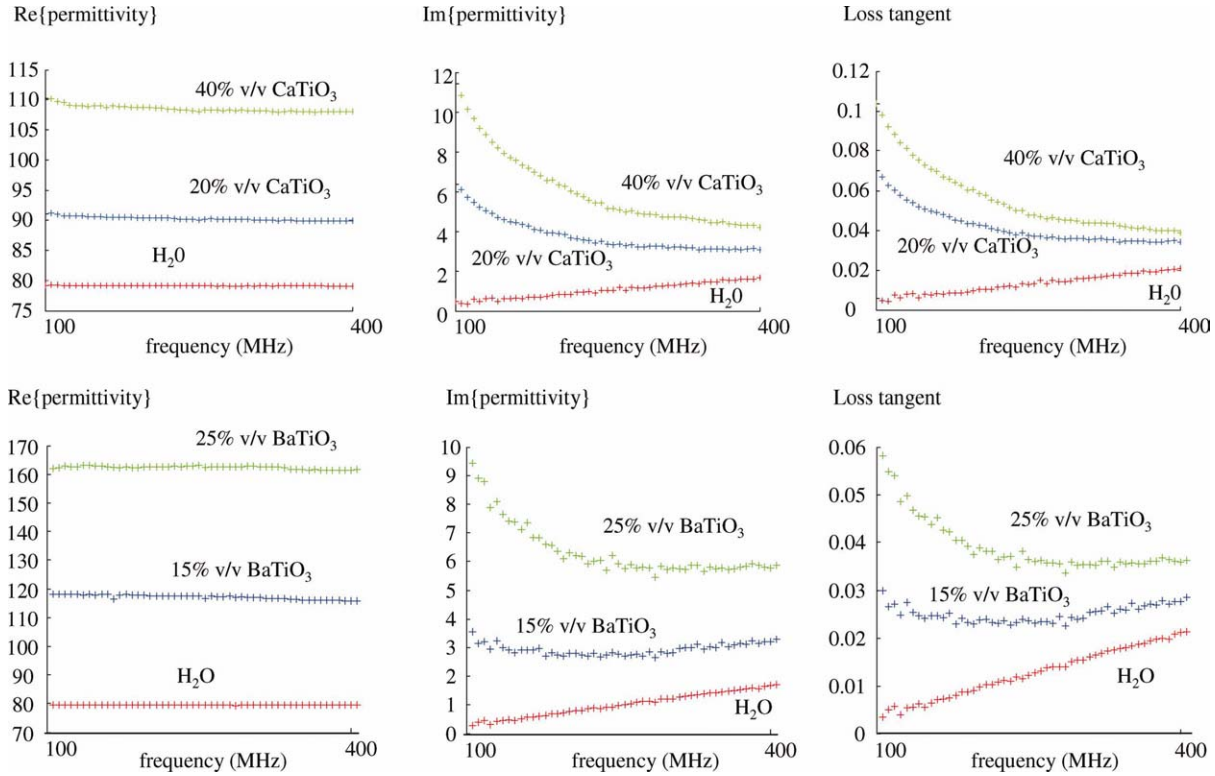

Figure 28 Plots of the real and imaginary components, as well as the derived loss tangent for water and different concentrations of calcium and barium titanates.

low background signal due primarily to short T_2 and T_2^* values, but also to a reduced water content, (iii) the possibility to essentially eliminate the background signal completely via the use of deuterated water, and (iv) the formation of a geometrically deformable but stable suspension (*68*).

$CaTiO_3$ is available as a fine powder with a density of ~4.1 g/cc. To form a suspension $CaTiO_3$ can be mixed with distilled, de-ionized water in volume/volume ratios up to 40%, at which point the suspension becomes saturated. Barium titanate is also available in fine powder form, but becomes saturated at a much lower volume/volume ratio of ~25%. The permittivities and loss tangents of the two types of suspension are shown as a function of frequency between 100 and 400 MHz in Figure 28. As can be seen, for pure water the real component of the permittivity does not vary very much with frequency, and the imaginary component is much smaller than the real one. The imaginary component, and therefore also the loss tangent, increases with frequency. This behavior is well-known, and has been described in detail in, for example, the context of very high field superconducting high-resolution NMR probe design (*69*). For the titanate suspensions, the real component is also quite independent of frequency above ~250 MHz, whereas the imaginary component decreases as a 1/f function for $CaTiO_3$ and is almost frequency independent for $BaTiO_3$. As the percentage of titanates increase both the real and imaginary components of the permittivity increase.

Theoretical values of permittivity as a function of the volume fraction can be calculated using Lichtenecker's logarithmic power law, Eq. [62], as shown in Figure 29. It should be noted that the data points corresponding to 10 and 15% $CaTiO_3$ do not fit the power law particularly well due to the physical difficulty of producing a stable suspension at such low concentrations of the powder: the probe measurements are made at the top of the suspension, so this means that the measured values are underestimates. These data are therefore not shown.

For the calcium titanate suspension the T_1 value for the dielectric pad was measured to be 110 ms, the T_2-value 12 ms, and the T_2^* value less than 2 ms. The shortening of the transverse relaxation times in a suspension is very familiar from the field of porous media magnetic resonance.

Both $CaTiO_3$ and $BaTiO_3$ suspensions have been used for imaging at 7 T. To maintain clinical utility in terms of high sensitivity and parallel imaging capability, a close-fitting 16-channel receive array

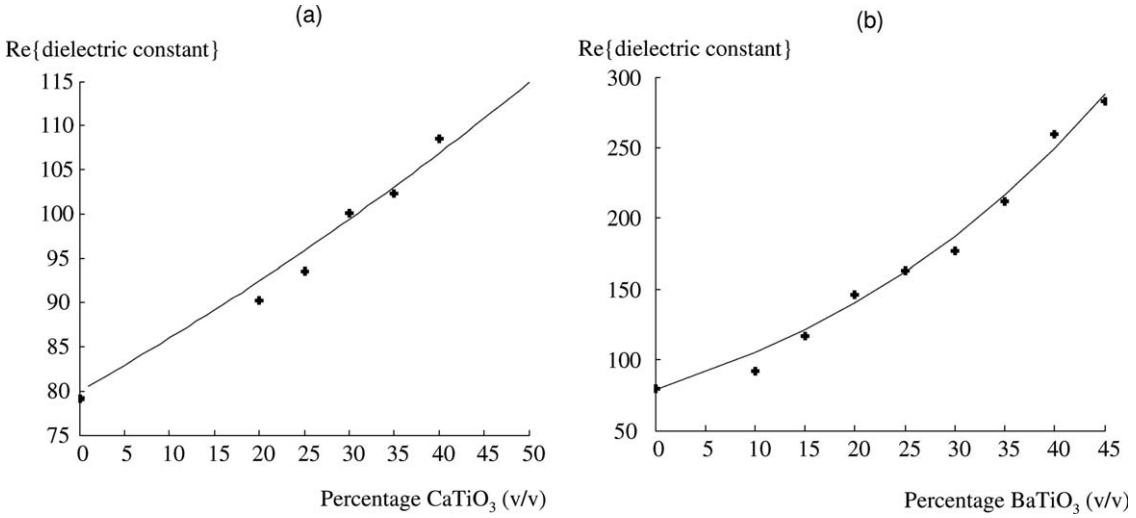

Figure 29 Plot of the real part of the permittivity vs. percentate calcium titanate (a) and barium titanate (b) in a suspension in deionized water. The closed circles represent measured data, with the dotted line being the closest fit from Lichtenecker's logarithmic power law.

consisting of eight radially gapped rows of z-overlapped coil pairs, with inner diameter 25.5 cm, was used as shown in Figure 30(a). As mentioned earlier, the lack of space means that only thin pads can be used in practice for brain scanning, and this is a potential advantage of high permittivity materials. Figures 30(b,c) shows simulations of the effect of placing two dielectric pads either side of the head, corresponding to the physical placement shown in Figure 30(a). The major effects are the significant increase in transmit field in the temporal lobes, which are typically areas of low signal intensity.

To understand the effects of the dielectric material one needs to consider the conduction (J_C) and displacement (J_D) current densities induced in the subject not only by the primary transmitted field but also the secondary fields generated by the dielectric material. Expanding on the definition of displacement current density given in Eq. [19]:

$$J_D = \varepsilon_0\varepsilon_r \frac{\partial E}{dt} = \varepsilon_0\varepsilon_r \frac{d}{dt}\left(E_0 e^{-j\omega t}\right) = -j\omega\varepsilon_0\varepsilon_r E \quad [63]$$

The total current density is given by:

$$J_{total} = J_C + J_D = \sigma E - j\omega\varepsilon_0\varepsilon_r E \quad [64]$$

As seen previously the ratio of the imaginary to real component of the permittivity depends both on conductivity and frequency:

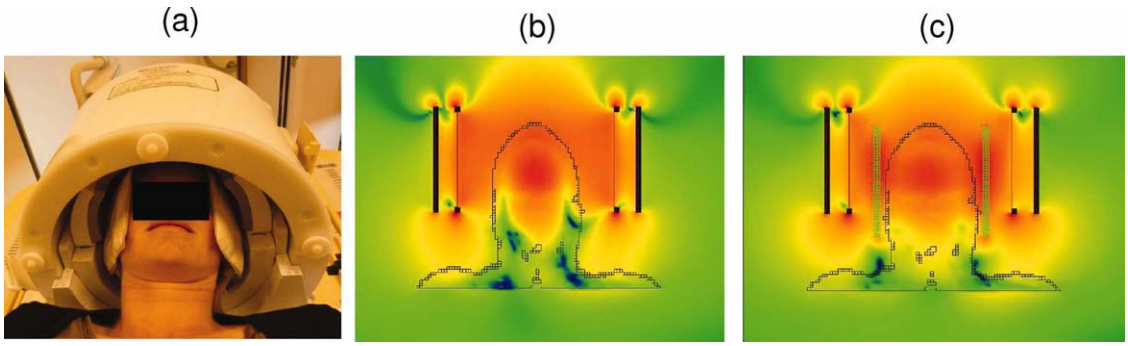

Figure 30 (a) Photograph of the physical setup used for experiments. Thin (8 mm) pads of suspensions of calcium titanate are placed either side of the head (the black bar is for patient anonymity). (b) Simulation of the B_1^+ component with no dielectric pads in place, the black outline represents the skin. (c) The B_1^+ component with the pads in place, showing a marked increase in field close to the temporal lobes.

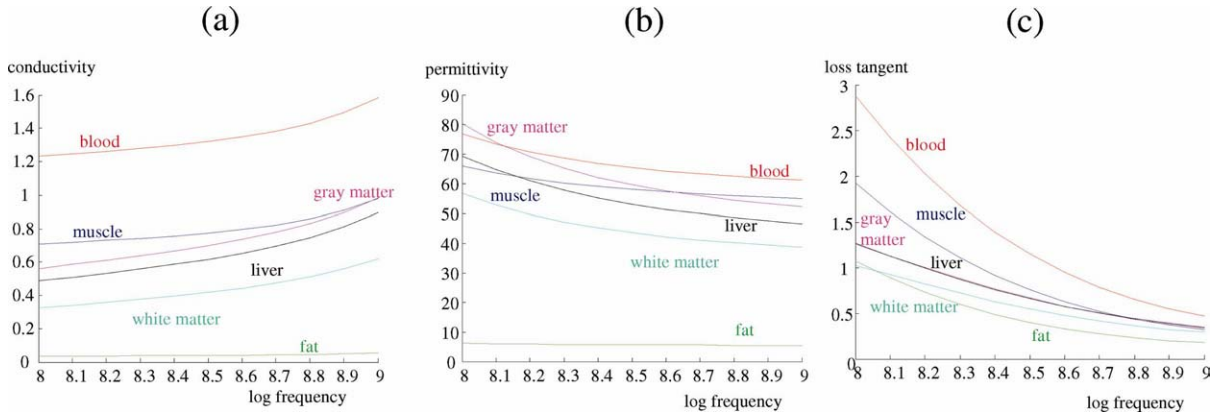

Figure 31 Plots of (a) conductivity (S/m), (b) relative permittivity and (c) loss tangent vs. frequency for different tissues. Values were derived from a fourth-order Cole–Cole fitted plot.

$$\varepsilon = \varepsilon' - j\frac{\sigma}{\omega} \qquad [65]$$

Values of conductivity, permittivity and loss tangent for different tissues are plotted in Figure 31. A full table of values at 7 T (300 MHz) is given in Appendix C. The ratio of conduction to displacement currents is given by:

$$\frac{J_c}{J_D} = \frac{\sigma}{\omega\varepsilon_r\varepsilon_0} \qquad [66]$$

For muscle ($\sigma = 0.77$ S/m, $\varepsilon_r = 58.2$) this ratio is ~0.7, for gray matter ($\sigma = 0.7$ S/m, $\varepsilon_r = 60$) ~0.6, and for lipid ($\sigma = 0.04$ S/m, $\varepsilon_r = 5.6$) ~0.4. So in tissue the displacement current has a slightly higher contribution than the conduction current, but both are important. However, for a high dielectric material with a loss factor of 0.05 and ε_r of 100, the ratio J_C/J_D is only 0.007, meaning that the displacement current is much higher than the conduction current, and effectively the conduction current can be ignored.

As an example, Figure 32 shows the z-component of the displacement current density in the human head without and with two thin (8 mm) pads of 40% v/v $CaTiO_3$ suspension placed either side of the head. In the situation without the dielectric pads there are nulls in the centre of the brain in the sagittal (a) and coronal (b) planes, and an asymmetric diagonal pattern in the axial plane (c). When the dielectric pads are added, there is a large displacement current induced within each pad, best seen in Figures 32(e,f), which changes quite significantly the displacement currents within the head itself, as shown in Figure 32(f).

In terms of practical applications of the high permittivity suspensions, Figure 33 shows the results of imaging and spectroscopy experiments at 7 T using two pads of 40% v/v calcium titanate placed next to the temporal lobes. MR spectroscopy of the temporal lobe is potentially extremely useful in studying a number of neurodegenerative diseases at clinical fields, but relatively low signal-to-noise has prevented reliable quantitation of, for example, glutamate and glutamine which are thought to play a key role in disease progression. As shown in Figure 33, the presence of the material increased the signal-to-noise ratio of the MR spectra by a factor-of-two without significantly reducing sensitivity in other areas of the brain, as shown by measured B_1^+ maps. An increase in the receive sensitivity, B_1^-, was also measured close to the pads. The spectral linewidth of the unsuppressed water peak within the voxel of interest was reduced slightly by the introduction of the dielectric pads (though not to a statistically significant degree). Using the LC model (*70*) for quantitative analysis of metabolite concentrations, the increase in S/N and slight decrease in spectral linewidth contributed to statistically significant reductions in the Cramer-Rao lower bounds (CRLB), also allowing the levels of glutamate and glutamine to be quantified with CRLBs below 20% (*71*).

Figure 34 shows a comparison of images acquired using clinical protocols optimized for 7 T obtained with and without the calcium titanate dielectric pads in place. In this case there was a single pad which covered both sides as well as the back of the head close to the cerebellum. The side-by-side sagittal comparison in Figure 34(a) shows a much higher signal intensity in the cerebellum, with significantly improved white matter/gray matter contrast indicating a higher tip angle and therefore increased transmit field. Axial slices show signal increases in the lateral brain. The coronal turbo-spin-echo (TSE) scans also show significant improvement in the signal in the cerebellar area.

Similar improvements in image quality can be obtained using a barium titanate suspension. Figure

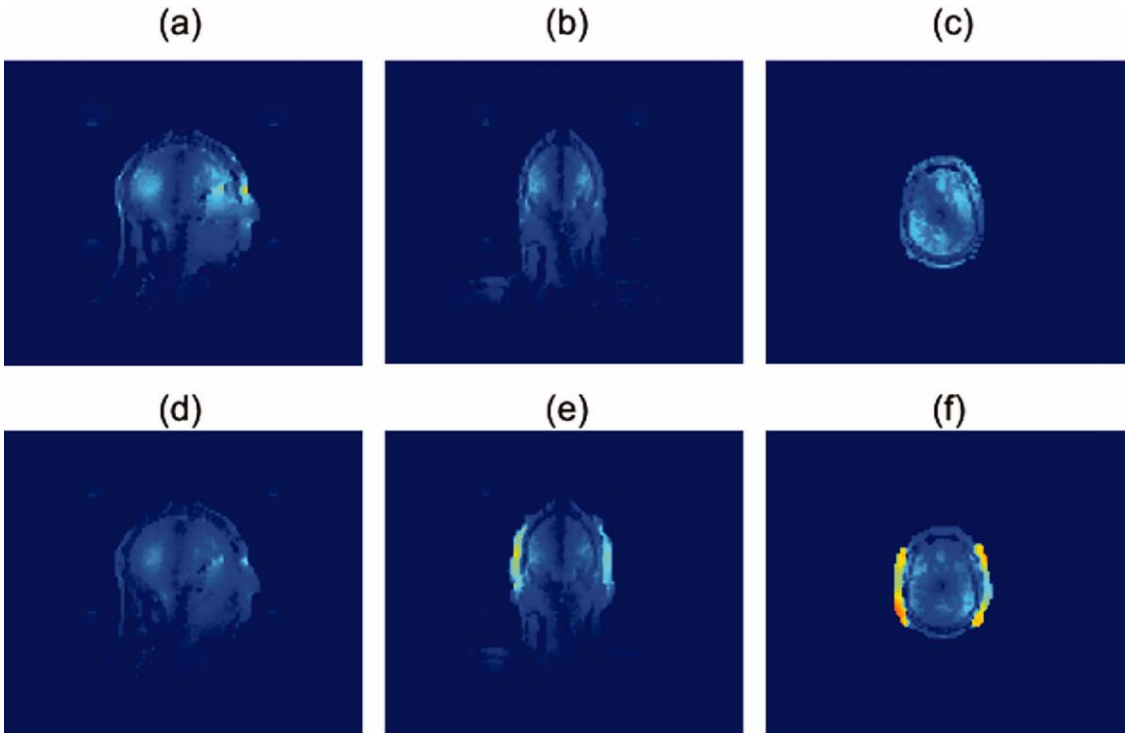

Figure 32 Electromagnetic simulations of the z-component of the displacement current within the head: (a), (b), and (c) no dielectric pads present: sagittal, coronal and axial views, respectively. (d), (e), and (f) corresponding images with two dielectric pads present on either side of the head.

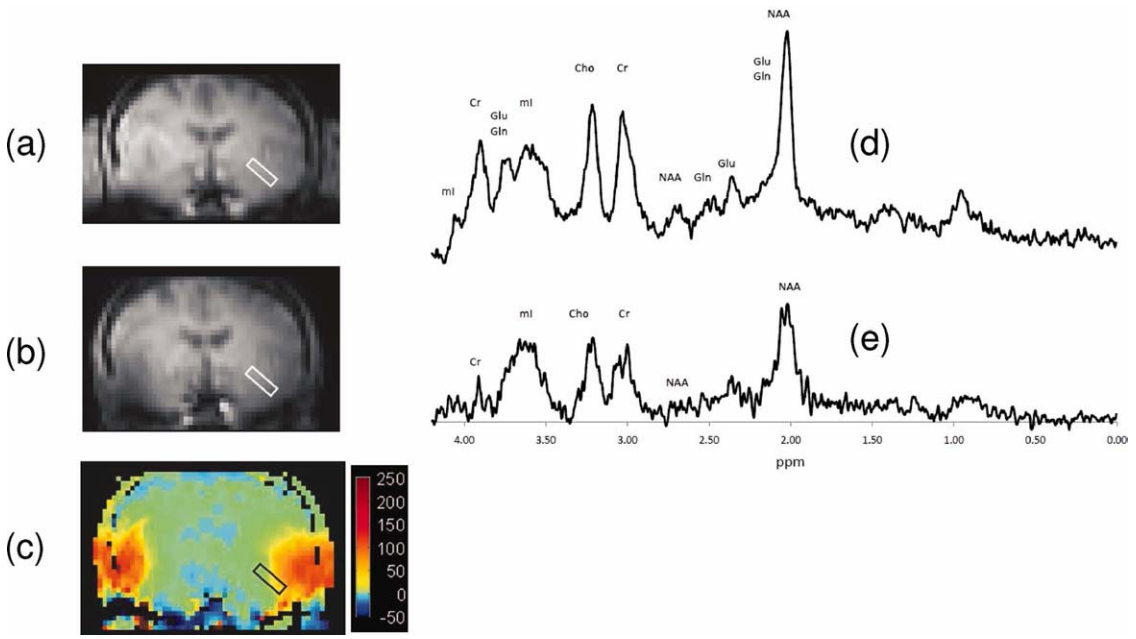

Figure 33 (a) Low-resolution magnitude image without dielectric pads used for B_1 mapping, (b) corresponding image with the pads in place. (c) Changes in the B_1^+ over the slice, measured as a percentage, showing significant increases in the spectroscopic voxel. ^{1}H NMR spectra acquired from the temporal lobe of the same subject with the dielectric material present (d) and without the pads (e).

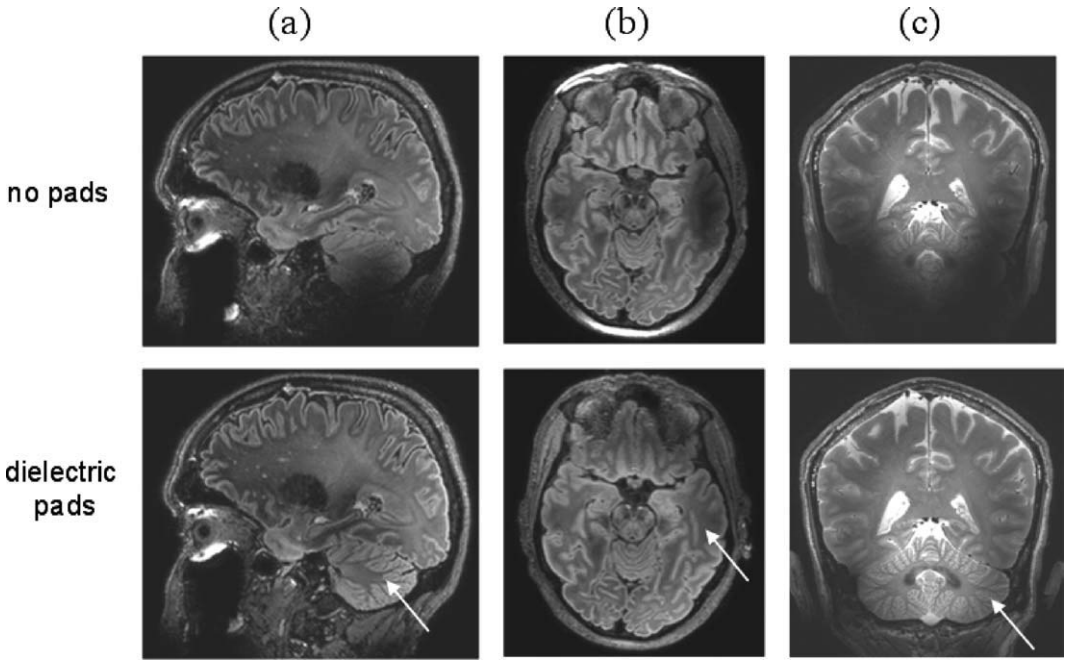

Figure 34 (a) Sagittal FLAIR scans, (b) reformatted axial FLAIR scans, and (c) axial TSE scans, all acquired without (top row) and with (bottom row) the dielectric pads present. Significant increases in S/N and image contrast produced by the dielectric pads are highlighted by the white arrows in the lower panels.

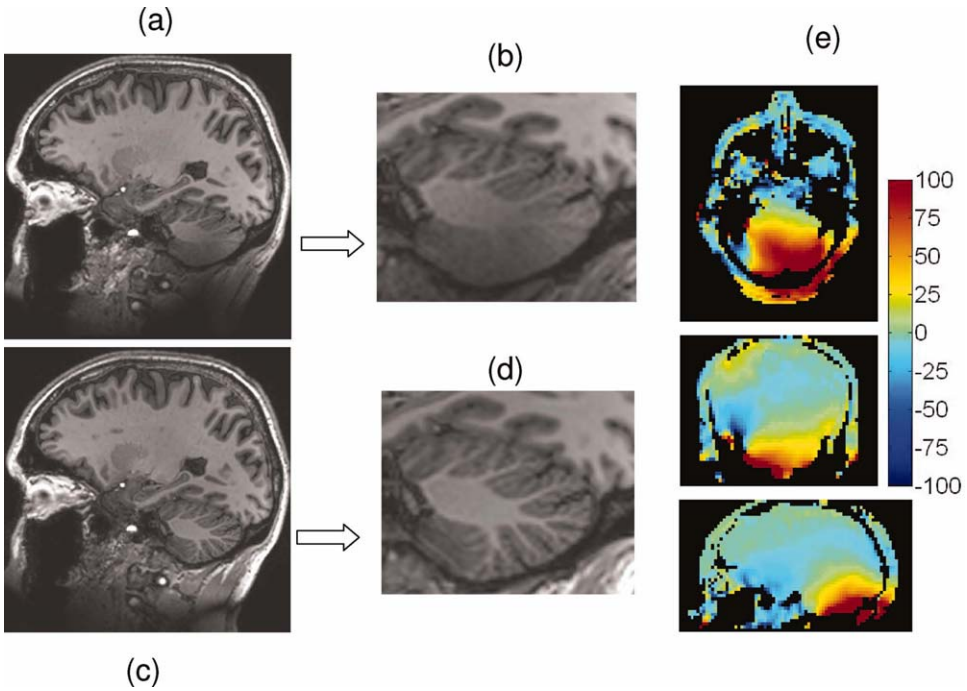

Figure 35 (a) Sagittal T_1-weighted image with no dielectric pads, (b) expansion of cerebellar region. (c) Corresponding image with barium titanate pad in place, and (d) expanded region showing much increased tissue contrast and S/N. (e) Measured percentage change in the B_1\plus field in all three directions.

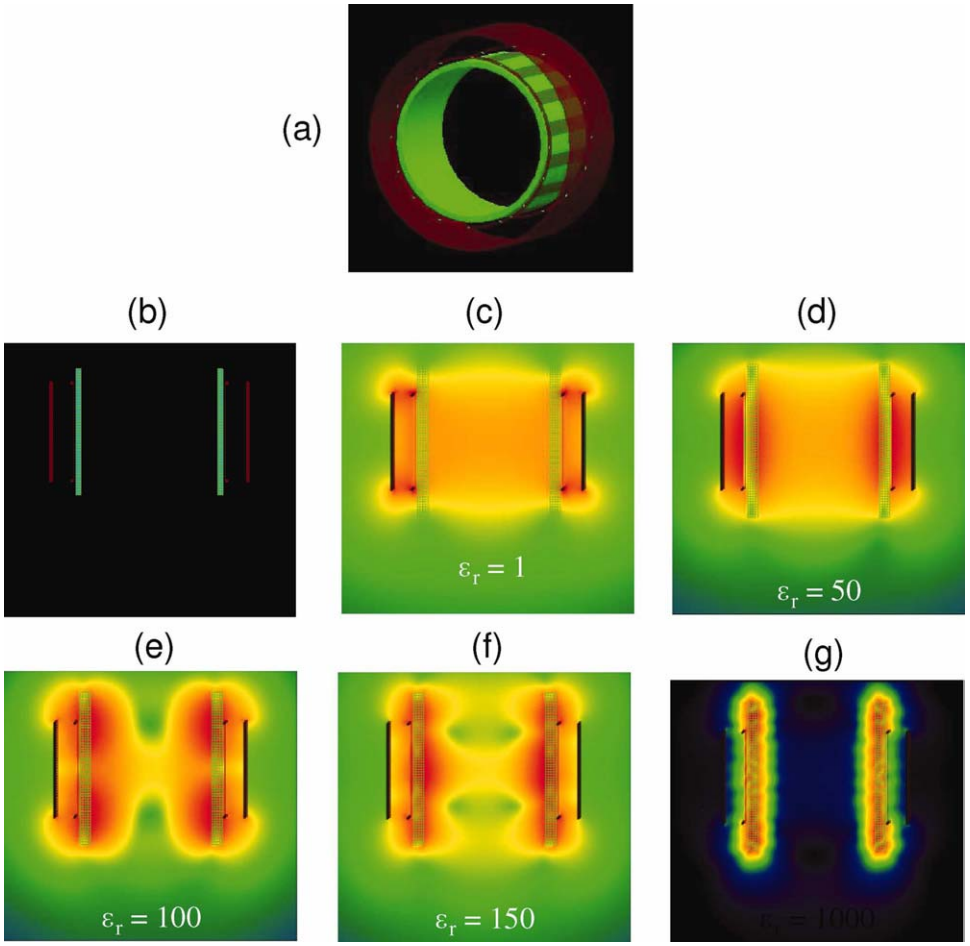

Figure 36 An illustration of the behavior of the B_1\plus transmit field from a 16 leg birdcage with materials with different permittivities placed in a cylindrical geometry inside the RF coil.

35 below shows results using a single pad placed behind the head of a volunteer. Increases of up to 100% in the B_1^+ at the posterior of the brain are shown, with corresponding improvements in S/N and image contrast in the cerebellum.

8. CONCLUSIONS AND FUTURE WORK

The use of high dielectric materials in magnetic resonance is a relatively recent area of research, although as outlined in this article, it builds upon a body of work in EPR which is over 20 years old. Dielectric materials can be used to form the MR resonator itself, or alternatively to shape the EM field by placing them around the sample/subject, or by integrating them into the RF coil itself. There are a number of areas in which one can imagine that this area could grow.

i. Dielectric resonators used for MR have so far only used materials with relatively low permittivities (150-330), and so for microsamples it would be extremely interesting to use materials with values in the thousands to tens of thousands. Manufacturing tolerances would be very tight, but extremely small resonators or arrays of resonators should be possible to construct.
ii. Optimizing geometries, shapes and material properties of dielectric pads for different clinical applications. From a simple point-of-view, a material with unity permittivity will have no effect of the RF field, whereas one with an extremely high value will simply contain the magnetic field within the material itself, and therefore decrease the overall field available for MR excitation. Therefore, an optimum value of the permittivity must exist, and this value will be different depending upon whether one wants to optimize the S/N and RF homogeneity over a large area such at the entire head or over a small localized

area close to the surface. As an example Figure 36 shows the transmit field as a function of the permittivity for a ring of material placed around the head. As expected, a very high permittivity is not useful. However, in these cases a single large structure should not be used, and an improved performance can be obtained by splitting the pad into smaller discrete elements.

iii. Another way in which high dielectrics might be useful is in targetting the RF energy provided by an external antenna in a technique known as "travelling wave MR" (*72*, *73*). In this technique the RF shield of the magnet bore acts like a waveguide, allowing the propagation of EM waves from an external antenna, provided that the dimensions and/or dielectric filling of the bore reduce the cutoff frequency to below the Larmor frequency. In practise this limits application to human scanners at 7 T and above. As shown in (*73*) the Poynting vector (which represents the direction of energy flow) diffracts whenever the EM encounters a high dielectric material (such as the body), and therefore by using low and high dielectrics it should be possible to "focus" the energy to specific areas.

ACKNOWLEDGMENTS

The authors acknowledge extremely about the useful discussions with a number of people including: Qing Yang, Chris Collins, Michael Lanagan, Chris Randall, and Kristina Haines at the Penn State University. Wouter Teeuwisse from the Leiden University Medical Center provided much input into the final document.

APPENDIX A

Table A1 Dielectric Properties of Selected Materials

Solvent	Electric Dipole Moment	Relative Permittivity
CCl_4	0	2.24
C_6H_6	0	2.28
CH_3CH_2OH	1.69	24.3
HCO_2H	1.41	58
H_2O	1.85	80
$HCONH_2$	3.73	109

Dielectric	Relative Permittivity	Temperature Dependence of the Relative Permittivity (ppm/°C)
TiO2 (rutile)	80–100	80
Calcium titanate	150–160	200
Strontium titanate	300	300
Strontium zirconate	60	12
Barium titanate[a]	2,000–10,000	40

[a]Values are highly dependent upon grain size and processing conditions for most dielectrics, and so these numbers are only intended to give an indication of the relative permittivity and temperature dependence.

APPENDIX B

DIELECTRIC RELAXATION

Dielectric relaxation refers to the time delay in the induction of molecular polarization which is caused by the application of an electric field. When the electric field is removed (or changes in the case of an alternating electric field) then there is a time associated with the molecule returning to its equilibrium state, and this time is called the relaxation time (τ). One can consider this to be analogous to time constants in voltage-driven RC and RL circuits, for example. In the case of low frequency electric fields, there is sufficient time for the dipoles to reach equilibrium between periods of the wave. This is not true at high frequencies, and the resulting time-lag leads to energy dissipation, i.e., the imaginary component of the permittivity increases. Mathematically the behavior in a pure liquid is described by the Debye equation.

$$\varepsilon(\omega) = \varepsilon'_{\omega=\infty} + \frac{\varepsilon'_{\omega=0} - \varepsilon'_{\omega=\infty}}{1 + j\omega\tau} \qquad [B1]$$

Figure B1(a) shows a plot of the real and imaginary components of the permittivity of water as a function of frequency. At frequencies well below relaxation, the rate of change of the alternating electric field is slow enough so that the dipole reorientations can keep pace. Therefore, the imaginary (lossy) component of the permittivity is linearly dependent upon frequency. As the frequency increases, so that there is now a time-lag between the dipole alignment and the changing electric field, the real component (representing energy storage) of the permittivity decreases rapidly. At frequencies

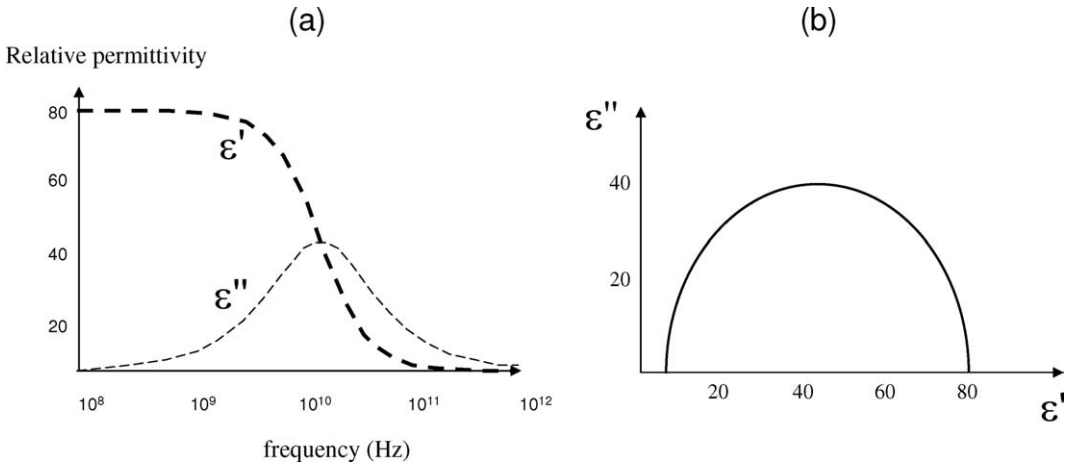

Figure B1 Behavior of the complex permittivity of water as a function of frequency. (a) values of real (bold lines) and imaginary (thin lines) follow the Debye equation. (b) the corresponding Cole–Cole plot.

well above the relaxation frequency, both real and imaginary components of the permittivity decrease, since orientation polarizability ceases to be an effective mechanism due to the dipole rotation effectively "not seeing" the much higher frequency fluctuations in the electric field. For the frequencies associated with NMR and MRI experiments the real component of the permittivity changes relative little from the DC value, but the imaginary component increases significantly. For high frequency EPR experiments the imaginary component can be significantly higher than the real component, leading to very high losses in aqueous samples. At still higher frequencies ($f > 10^{12}$ Hz) other mechanisms of relaxation occur involving resonant behavior associated with ionic polarization, but these are not relevant for MR or EPR measurements.

The Debye equation only holds for certain samples. A generalization of the Debye equation is the Cole–Cole equation, which can be used for water-containing substances:

$$\varepsilon(\omega) = \varepsilon'_{\omega=\infty} + \frac{\varepsilon'_{\omega=0} - \varepsilon'_{\omega=\infty}}{1 + (j\omega\tau)^{1-\alpha}} \qquad [B2]$$

where $0 < \alpha < 1$, which of course becomes the Debye equation when $\alpha = 0$. Figure B1(b) shows a typical Cole–Cole plot, which lots the real vs. imaginary component of the permittivity, and which is a semicircle for materials with a single relaxation frequency. The peak of the loss factor, i.e., the highest point on the vertical axis, corresponds to the relaxation frequency.

APPENDIX C

Conductivities and Permittivities of Biological Tissue at 300 mhz

Tissue	Conductivity (S/m)	Relative Permittivity
Skin	49.8	0.64
Tendon	48.0	0.54
Fat	5.6	0.04
Cortical bone	13.4	0.08
Cancellous bone	23.2	0.22
Blood	65.7	1.32
Muscle	58.2	0.77
Gray matter	60.0	0.69
White matter	43.8	0.41
Cerebrospinal fluid	72.7	2.22
Cerebellum	59.7	0.97
Sclera	58.9	0.98
Vitreous humor	69.0	1.52
Nerve	36.9	0.42
Cartilage	46.8	0.55
Tongue	58.9	0.74
Stomach	68.7	0.97
Lung	24.8	0.36

REFERENCES

1. Kraus JD, Fleisch DA. 1999. Electromagnetics with Applications, Chapters 4 and 7. McGraw-Hill.
2. Galasso FS. 1969. Structure Properties and Preparation of Perovskite Type Compounds. Oxford: Pergamon Press. 3 p.
3. Buessem WR, Cross LE, Goswami AK. 1966. Phenomenological theory of high permittivity in

fine-grained barium titanate. J Am Cer Soc 49: 33–36.
4. von Hippel AR. 1954. Dielectric Materials and Applications. New York: MIT Technical and John Wiley.
5. Nalwa H. 1999. Handbook of low and high dielectric constant materials and their applications. London, UK: Academic Press.
6. Glisson AW. 1986. Dielectric resonators. In: Kajfez D,Guillon P, eds. Norwood, Massachusetts: Artech House.
7. Fiedzius S, Jelenski A. 1971. Influence of conducting walls on resonant frequencies of dielectric microwave resonator. IEEE Trans Microwave Theory Tech MT19:778.
8. Pospieszalski MW. 1979. Cylindrical dielectric resonators and their applications in tem line microwave circuits. IEEE Trans Microwave Theory Tech 27:233–238.
9. Jaworski M, Sienkiewicz A, Scholes CP. 1997. Double-stacked dielectric resonator for sensitive EPR measurements. J Magn Reson 124:87–96.
10. Gurevich VL, Tagantsev AK. 1991. Intrinsic dielectric loss in crystals. Adv Phys 40:719–767.
11. Walsh WM, Rupp LW. 1986. Enhanced electron-spin-resonance sensitivity using a dielectric resonator. Rev Sci Instrum 57:2278–2279.
12. Hakki BW, Coleman PD. 1960. A dielectric resonator method of measuring inductive capacities in the millimeter range. Microwave Theory Tech IRE Trans 8:402–410.
13. Cohn SB, Kelly KC. 1966. Microwave measurement of high-dielectric-constant materials. IEEE Trans Microwave Theory Tech MT14:406.
14. Courtney WE. 1970. Analysis and evaluation of a method of measuring complex permittivity and permeability of microwave insulators. IEEE Trans Microwave Theory Tech MT18:476.
15. Kobayashi Y, Katoh M. 1985. Microwave measurement of dielectric-properties of low-loss materials by the dielectric rod resonator method. IEEE Trans Microwave Theory Tech 33:586–592.
16. Annino G, Cassettari M, Longo I, Martinelli M. 1999. Dielectric resonators in ESR: overview, comments and perspectives. Appl Magn Reson 16:45–62.
17. Carter DL, Okaya A. 1960. Electron paramagnetic resonance of Fe-3 in Tio2 (Rutile). Phys Rev 118: 1485–1490.
18. Okaya A. 1960. The rutile microwave resonator. Proc Inst Radio Eng 48:1921.
19. Rosenbaum FJ. 1964. Dielectric cavity resonator for ESR experiments. Rev Sci Instrum 35:1550–1554.
20. Harthhoorn JL, Smidt J. 1969. Dielectric cavity resonator applied to electron spin resonance. Appl Sci Res 20:148–160.
21. Dykstra RW, Markham GD. 1986. A dielectric sample resonator design for enhanced sensitivity of electron paramagnetic resonance spectroscopy. J Magn Reson 69:350–355.
22. Bromberg SE, Chan IY. 1992. Enhanced sensitivity for high-pressure EPR using dielectric resonators. Rev Sci Instrum 63:3670–3673.
23. Sakai N, Pifer JH. 1985. Electron-paramagnetic resonance at high-pressure using a diamond anvil cell. Rev Sci Instrum 56:726–731.
24. Sienkiewicz A, Qu KB, Scholes CP. 1994. Dielectric resonator-based stopped-flow electron-paramagnetic-resonance. Rev Sci Instrum 65:68–74.
25. Lassmann G, Schmidt PP, Lubitz W. 2005. An advanced EPR stopped-flow apparatus based on a dielectric ring resonator. J Magn Reson 172:312–323.
26. Wen H, Jaffer FA, Denison TJ, Duewell S, Chesnick AS, Balaban RS. 1996. The evaluation of dielectric resonators containing H2O or D2O as RF coils for high-field MR imaging and spectroscopy. J Magn Reson Ser B 110:117–123.
27. Neuberger T, Tyagi V, Semouchkina E, Lanagan M, Baker A, Haines K, et al. 2008. Design of a ceramic dielectric resonator for NMR microimaging at 14.1 tesla. Concept Magn Reson Part B: Magn Reson Eng 33B:109–114.
28. Haines K, Neuberger T, Lanagan M, Semouchkina E, Webb AG. 2009. High Q calcium titanate cylindrical dielectric resonators for magnetic resonance microimaging. J Magn Reson 200:349–353.
29. Foo TK, Hayes CE, Kang YW. 1992. Reduction of RF penetration effects in high field imaging. Magn Reson Med 23:287–301.
30. Gabriel C, Gabriel S, Corthout E. 1996. The dielectric properties of biological tissues: I. Literature survey. Phys Med Biol 41:2231–2249.
31. Gabriel S, Lau RW, Gabriel C. 1996. The dielectric properties of biological tissues: III. Parametric models for the dielectric spectrum of tissues. Phys Med Biol 41:2271–2293.
32. Gabriel S, Lau RW, Gabriel C. 1996. The dielectric properties of biological tissues: II. Measurements in the frequency range 10 Hz to 20 GHz. Phys Med Biol 41:2251–2269.
33. Foo TK, Hayes CE, Kang YW. 1991. An analytical model for the design of RF resonators for MR body imaging. Magn Reson Med 21:165–177.
34. Butterworth EJ, Walsh EG, Hugg JW. 2001. TiO2 dielectric filled toroidal radio frequency cavity resonator for high-field NMR. NMR Biomed 14:184–191.
35. Gor'kov PL, Witter R, Chekmenev EY, Nozirov F, Fu R, Brey WW. 2007. Low-E probe for (19)F-(1)H NMR of dilute biological solids. J Magn Reson 189:182–189.
36. Gor'kov PL, Chekmenev EY, Li C, Cotten M, Buffy JJ, Traaseth NJ, et al. 2007. Using low-E resonators to reduce RF heating in biological samples for static solid-state NMR up to 900 MHz. J Magn Reson 185:77–93.
37. McNeill SA, Gor' kov PL, Shetty K, Brey WW, Long JR. 2009. A low-E magic angle spinning probe

for biological solid state NMR at 750 MHz. J Magn Reson 197:135–144.
38. Grant CV, Wu CH, Opella SJ. 2010. Probes for high field solid-state NMR of lossy biological samples. J Magn Reson 204:180–188.
39. Stringer JA, Bronnimann CE, Mullen CG, Zhou DH, Stellfox SA, Li Y, et al. 2005. Reduction of RF-induced sample heating with a scroll coil resonator structure for solid-state NMR probes. J Magn Reson 173:40–48.
40. Crum LA, Zilm KW. 2007. Resonator designs for decreasing sample heating in solid state NMR experiments. Presented at the Exp NMR Conf, Asilomar, April 2007.
41. Neufeld A, Landsberg N, Boag A. 2009. Dielectric inserts for sensitivity and RF magnetic field enhancement in NMR volume coils. J Magn Reson 200:49–55.
42. Webb AG, Collins CM. 2010. Parallel transmit and receive technology in high-field magnetic resonance neuroimaging. Int J Imaging Syst Technol 20:2–13.
43. Collins CM, Smith MB. 2001. Calculations of B1 distribution, SNR, and SAR for a surface coil adjacent to an anatomically-accurate human body model. Magn Reson Med 45:692–699.
44. Collins CM, Yang B, Yang QX, Smith MB. 2002. Numerical calculations of the static magnetic field in three-dimensional multi-tissue models of the human head. Magn Reson Imaging 20:413–424.
45. Collins CM, Yang QX, Wang JH, Zhang X, Liu H, Michaeli S, et al. 2002. Different excitation and reception distributions with a single-loop transmit-receive surface coil near a head-sized spherical phantom at 300 MHz. Magn Reson Med 47:1026–1028.
46. Wang J, Yang QX, Zhang X, Collins CM, Smith MB, Zhu XH, et al. 2002. Polarization of the RF field in a human head at high field: a study with a quadrature surface coil at 7.0 T. Magn Reson Med 48:362–369.
47. Collins CM, Liu W, Wang J, Gruetter R, Vaughan JT, Ugurbil K, et al. 2004. Temperature and SAR calculations for a human head within volume and surface coils at 64 and 300 MHz. J Magn Reson Imaging 19:650–656.
48. Wang Z, Lin JC, Mao W, Liu W, Smith MB, Collins CM. 2007. SAR and temperature: simulations and comparison to regulatory limits for MRI. J Magn Reson Imaging 26:437–441.
49. IEC. 2002. International standard, medical equipment—part 2: particular requirements for the safetyof magnetic resonance equipment for medical diagnosis, 2nd revision. International Electrotechnical Commission Brussels 601–2-33.
50. Metzger GJ, Snyder C, Akgun C, Vaughan T, Ugurbil K, van de Moortele PF. 2008. Local B1 shimming for prostate imaging with transceiver arrays at 7T based on subject-dependent transmit phase measurements. Magn Reson Med 59:396–409.
51. Vaughan T, DelaBarre L, Snyder C, Tian J, Akgun C, Shrivastava D, et al. 2006. 9.4T human MRI: preliminary results. Magn Reson Med 56:1274–1282.
52. Zelinski AC, Wald LL, Setsompop K, Alagappan V, Gagoski BA, Goyal VK, et al. 2008. Fast slice-selective radio-frequency excitation pulses for mitigating B1 inhomogeneity in the human brain at 7 tesla. Magn Reson Med 59:1355–1364.
53. Franklin KM, Dale BM, Merkle EM. 2008. Improvement in B1-inhomogeneity artifacts in the abdomen at 3T MR imaging using a radiofrequency cushion. J Magn Reson Imaging 27:1443–1447.
54. Sreenivas A, Lowry M, Gibbs P, Pickles M, Turnbull LW. 2007. A simple solution for reducing artefacts due to conductive and dielectric effects in clinical magnetic resonance imaging at 3 T. Eur J Radiol 62:143–146.
55. Takayama Y, Nonaka H, Nakajima M, Obata T, Ikehira H. 2008. Reduction of a high-field dielectric artifact with homemade gel. Magn Reson Med Sci 7:37–41.
56. Sunaga T, Ikehira H, Furukawa S, Tamura M, Yoshitome E, Obata T, Shinkai H, Tanada S, Murata H, Sasaki Y. 2003. Development of a dielectric equivalent gel for better impedance matching for human skin. Bioelectromagnetics 24:214–217.
57. Sled JG, Pike GB. 1998. Standing-wave and RF penetration artifacts caused by elliptic geometry: an electrodynamic analysis of MRI. IEEE Trans Med Imaging 17:653–662.
58. Yang QX, Mao W, Wang J, Smith MB, Lei H, Zhang X, Ugurbil K, Chen W. 2006. Manipulation of image intensity distribution at 7.0 T: passive RF shimming and focusing with dielectric materials. J Magn Reson Imaging 24:197–202.
59. Oster G. 1946. The dielectric properties of liquid mixtures. J Am Chem Soc 68:2036–2041.
60. Harvey AH, Prausnitz JM. 1987. Dielectric-constants of fluid mixtures over a wide-range of temperature and density. J Solution Chem 16:857–869.
61. Sihvola A. 2000. Mixing rules with complex dielectric coefficients. Subsurface Sensing Technol Appl 1:393–415.
62. Simpkin R. 2010. Derivation of Lichtenecker's logarithmic mixture formula from Maxwell's equations. IEEE Trans Microwave Theory Tech 58:545–550.
63. Goncharenko AV, Lozovski VZ, Venger EF. 2000. Lichtenecker's equation: applicability and limitations. Opt Commun 174:19–32.
64. Vo HT, Shi FG. 2002. Towards model-based engineering of optoelectronic packaging materials: dielectric constant modeling. Microelectron J 33:409–415.
65. Tuncer E, Serdyuk YV, Gubanski SM. 2002. Dielectric mixtures: electrical properties and modeling. IEEE Trans Dielect Elect Insul 9:809–828.
66. Tuncer E, Nettelblad B, Gubanski SM. 2002. Non-Debye dielectric relaxation in binary dielectric

mixtures (50–50): randomness and regularity in mixture topology. J Appl Phys 92:4612–4624.
67. Tuncer E. 2004. Signs of low frequency dispersions in disordered binary dielectric mixtures (fifty-fifty). J Phys D: Appl Phys 37:334–342.
68. Haines K, Smith NB, Webb AG. 2010. New high dielectric constant materials for tailoring the B-1() distribution at high magnetic fields. J Magn Reson 203:323–327.
69. Horiuchi T, Takahashi M, Kikuchi J, Yokoyama S, Maeda H. 2005. Effect of dielectric properties of solvents on the quality factor for a beyond 900 MHz cryogenic probe model. J Magn Reson 174:34–42.
70. Provencher SW. 1993. Estimation of metabolite concentrations from localized in vivo proton NMR spectra. Magn Reson Med 30:672–679.
71. Snaar JE, Teeuwisse WM, Versluis MJ, van Buchem MA, Kan HE, Smith NB, et al. 2010. Improvements in high-field localized MRS of the medial temporal lobe in humans using new deformable high-dielectric materials. NMR Biomed. DOI: 10.1002/nbm.1638
72. Brunner DO, De ZN, Frohlich J, Paska J, Pruessmann KP. 2009. Travelling-wave nuclear magnetic resonance. Nature 457:994–998.
73. Webb AG, Collins CM, Versluis MJ, Kan HE, Smith NB. 2010. MRI and localized proton spectroscopy in human leg muscle at 7 T using longitudinal traveling waves. Magn Reson Med 63: 297–302.

BIOGRAPHIES

Andrew Webb received his Bachelors degree in Chemistry from the University of Bristol in 1986 and his Ph.D. from the University of Cambridge in 1989. He is currently a Full Professor in the Department of Radiology at the Leiden University Medical Center in The Netherlands, and is Director of the C.J. Gorter Center for High Field Magnetic Resonance Imaging. His major area of research is the development of new engineering techniques for clinical applications of high field MRI.